In-depth immunophenotyping with mass cytometry during TB treatment reveals non-canonical T-cell subsets associated with sputum culture conversion.

Authors: Carole CHEDID[1,2,3#], Thibault ANDRIEU[4], Eka KOKHREIDZE[5#], Nestani TUKVADZE[5#], Samanta BISWAS[6#], Md. Fahim ATHER[6#], Mohammad Khaja Mafij UDDIN[6#], Sayera BANU[6#], Flavio DE MAIO[7], Giovanni DELOGU[7], Hubert ENDTZ[8#], Delia GOLETTI[9], Marc VOCANSON[1], Oana DUMITRESCU[1,10,11], Jonathan HOFFMANN[1,2*#], Florence ADER[1,12*].

Affiliations:

1. Centre International de Recherche en Infectiologie, Legionella Pathogenesis Group, INSERM U1111, Université Claude Bernard Lyon 1, CNRS UMR5308, École Normale Supérieure de Lyon, Lyon, France
2. Medical and Scientific Department, Fondation Mérieux, Lyon, France
3. Département de Biologie, Ecole Normale Supérieure de Lyon, Lyon, France
4. Cytometry Core Facility, Centre de Recherche en Cancérologie de Lyon, Université Claude Bernard Lyon 1, Inserm 1052, CNRS 5286, Centre Léon Bérard, 69373, Lyon, France
5. National Center for Tuberculosis and Lung Diseases (NCTBLD), Tbilisi, Georgia
6. Infectious Diseases Division, International Centre for Diarrhoeal Disease Research, Bangladesh (icddr,b), Dhaka, Bangladesh
7. Dipartimento di Scienze biotecnologiche di base, cliniche intensivologiche e perioperatorie – Sezione di Microbiologia, Università Cattolica del Sacro Cuore, Rome, Italy
8. Fondation Mérieux, Lyon, France

9. Translational Research Unit, Department of Epidemiology and Preclinical Research, "L. Spallanzani" National Institute for Infectious Diseases (INMI), IRCCS, Rome, Italy

10. Hospices Civils de Lyon, Institut des Agents Infectieux, Laboratoire de Bactériologie, Lyon, France

11. Université Lyon 1, Facultés de Médecine et de Pharmacie de Lyon, Lyon, France

12. Hospices Civils de Lyon, Hôpital de la Croix-Rousse, Département des Maladies Infectieuses et Tropicales, F-69004, Lyon, France.

* These authors share the senior authorship.

#: On behalf of the HINTT working group within the GABRIEL network.

Keywords: tuberculosis; treatment monitoring; immunophenotyping; $CD8^+$ T-cells; heparin-binding hemagglutinin; inflammatory markers; mass cytometry; unsupervised data analysis.

Corresponding author:

Carole CHEDID

Centre International de Recherche en Infectiologie – INSERM U1111 – CNRS UMR5308

Département des Maladies Infectieuses et Tropicales

Hôpital de la Croix-Rousse, Hospices Civils de Lyon,

104, Grande Rue de la Croix-Rousse

69004 Lyon, FRANCE

carole.chedid@fondation-merieux.org

+33 6 72 68 69 35

Summary

In patients treated for pulmonary TB, high-dimensional immune profiling with mass cytometry revealed that *Mycobacterium tuberculosis* culture conversion is associated with newly characterized peripheral $CD8^+$ T-cell phenotypes. This paves the way for new immune biomarkers associated with mycobacterial sterilization.

Abstract

Tuberculosis (TB) is a difficult-to-treat infection because of multidrug regimen requirements based on drug susceptibility profiles and treatment observance issues. TB cure is defined by mycobacterial sterilization, technically complex to systematically assess. We hypothesized that microbiological outcome was associated with stage-specific immune changes in peripheral whole blood during TB treatment. The T-cell phenotypes of treated TB patients were prospectively characterized in a blinded fashion using mass cytometry after *Mycobacterium tuberculosis* (*Mtb*) antigen stimulation, and then correlated to sputum culture status. At two months of treatment, cytotoxic and terminally differentiated $CD8^+$ T-cells were under-represented and naïve $CD4^+$ T-cells were over-represented in positive- *versus* negative-sputum culture patients, regardless of *Mtb* drug susceptibility. At treatment completion, an antigen-driven T-cell immune shift towards differentiated subpopulations was associated with TB cure. Overall, we identified specific T-cell profiles associated with slow sputum converters, which brings new insights in TB prognostic biomarker research designed for clinical application.

Introduction

Tuberculosis (TB) is a leading cause of death of infectious origin, responsible for 1.5 million deaths worldwide in 2020 (World Health Organization Geneva, 2020). TB treatment regimens have toxic side effects (World Health Organization Geneva, 2019) requiring monitoring throughout treatment to adapt it and assess effectiveness. Pulmonary TB treatment monitoring relies on *Mycobacterium tuberculosis* (*Mtb*) detection in sputum samples (World Health Organization Geneva, 2018), which can be difficult to collect in later stages of treatment (Singhania et al., 2018). Smear microscopy yields highly sample- and operator-dependent results and has poor sensitivity (Parrish and Carroll, 2011). Sputum culture is the gold standard, although slow and requiring biosafety laboratory environments (Horne et al., 2010). Simultaneously, one of the main stakes in improving TB management is shortening TB treatment (Lienhardt et al., 2016). Overall, there is a need for novel non-sputum-based tools to monitor disease resolution and assess cure while remaining feasible in primary care settings (Goletti et al., 2018). Blood-based host immune biomarkers have recently gained interest in TB research as immune cells undergo phenotypic changes throughout the disease. Numerous past investigations have pointed to variations in the abundance and marker expression of several targeted subpopulations (Ahmed et al., 2018b; Adekambi et al., 2015a; Goletti et al., 2006b; Agrawal et al., 2018), in particular T-cells, which are pivotal effectors for *Mtb* clearance (Riou et al., 2020). However, this has been explored mostly in low-TB prevalence settings or with conventional flow cytometry, targeting a limited number of cell markers (Chiacchio et al., 2017; Musvosvi et al., 2018).

High-dimensional single-cell technologies such as mass cytometry enable the detection and quantification of a high number of cell markers (Gossez et al., 2018). This technique bypasses the limitations of spectral overlap by using monoclonal antibodies coupled to metal polymers, and has allowed high-dimensional exploration of the immune landscape in several domains

(Kourelis et al., 2019; Rubin et al., 2019). It has been applied to immune profiling during TB treatment in a 2018 study by Roy Chowdhury and colleagues (Roy Chowdhury et al., 2018), in which the authors have provided a general overview of changes in the main immune blood cells during treatment.

Here, in a prospective, international cohort study of adult patients treated for pulmonary TB in high prevalence countries, peripheral blood T-cell immune-profiles were characterized using a 29-marker mass cytometry panel. In-depth T-cell phenotypical analysis was performed upon TB treatment initiation, after two months and at completion of treatment. To examine the relation between mycobacterial clearance in hosts and changes in T-cell immune-profiles, the results of these analysis were compared in negative and positive sputum culture conversion patients after two months of treatment.

Results

Study design and analysis strategy

Between May 2019 and July 2020, 144 cell samples collected from 22 adult TB patients were analyzed (Bangladesh, n=4 and Georgia, n=18; DS- and DR-TB, n=11 each) (Supp. Figure 1). Patient demographic, microbiological and clinical characteristics are available in Supp. Table 1. All patients achieved microbiological cure at the end of treatment, but were retrospectively classified into two response groups according to their *M. tuberculosis* culture status at T1 (after two months of treatment): fast converters (n=18; negative culture at T1 and T2) and slow converters (n=4; positive culture at T1 and negative culture at T2). Among the latter, three patients were treated for DS-TB and one for DR-TB.

An overview of the data collection and analysis process is shown in Figure 1. Briefly, data from all samples were clustered automatically into subsets of homogeneous phenotypes to provide a framework for analysis. Clusters were then color-coded and plotted onto a two-dimension map

to create a visual reference used throughout the paper (Figure 2). On this basis, automatically detected clusters were first quantified and analyzed dynamically throughout treatment to identify median clusters abundance variations associated with treatment completion (Figure 3). Cluster phenotypes were deduced from marker expression heatmaps, and hierarchical clustering was applied based on marker expression (Figure 4). In a supervised manner, clusters of similar abundance changes and immunophenotypes were then re-grouped into larger subsets, in order to assess relevance of the detected abundance variations at the individual level, and consistency with manual gating (Figure 5). Finally, a cross sectional analysis was performed at T1 to identify which automatically detected clusters differentiated patients based on the microbiological response to the intensive phase of treatment (*Mtb* culture positivity at T1; Figures 6 and 7).

Overall analysis of peripheral T lymphocyte subset abundance changes throughout TB treatment.

First, a phenotype analysis was performed to identify the main expected T-cell subpopulations. As no apparent difference was seen in UMAP structures within samples from the different timepoints and stimulation conditions despite some marker expression differences between stimulation conditions (Supp. Figure 2; exact p-values and test statistics in Supp. Table 2), we performed the phenotype analysis on all single $CD3^+$ events. The purpose of this study was not to compare the stimulations, but rather to use them to uncover clusters that might be associated with treatment response and that would not be visible in unstimulated samples. FlowSOM automated clustering was performed on $CD3^+$ events, revealing a total of 196 automatically detected clusters (Figure 2.A to 2.C). They were automatically grouped into 18 meta-clusters, which were assembled into 12 canonical T-cell subpopulations in a supervised manner (Figure

2.D and 2.E). FlowSOM clusters and meta-clusters were then visualized on the initial UMAP to create a reference map of all automatically detected T-cell subsets (Figure 2.F and 2.G).

To initiate the abundance analysis, variations of the main T-cell subpopulations throughout treatment were then studied using a stratification according to each stimulation condition. No significant change in the proportion of total $CD4^+$, $CD8^+$, γδ, double negative (DN, $CD4^-$ $CD8^-$) or double positive (DP, $CD4^+$ $CD8^+$) T-cells was observed throughout treatment in any stimulation condition (Supp. Figure 3). For all main studied subpopulations, no significant difference was observed between DS- and DR-TB patients (data not shown).

Differential abundance of non-canonical T-cell subsets throughout TB treatment.

To identify non-canonical T-cell subsets whose abundance changed throughout treatment, we calculated the percentage of each automatically determined FlowSOM cluster at each timepoint and in each stimulation condition. These clusters were then categorized into two groups: enriched or decreased after treatment completion. Abundance changes were studied between T0 and T1 and T0 and T2 to characterize the main clusters associated with response to treatment intensive phase and with treatment completion respectively. As these clusters represent non-canonical cell subpopulations, their frequencies among total $CD3^+$ events were low (< 5% in most samples). Hence, the differences analyzed thereafter describe rare populations and warrant cautious analysis.

When comparing the reference UMAP (Figure 2.G) to the UMAP of clusters which were increased between T0 and T1 (Supp. Figure 4.A), we observed that they were either DN T-cells, or effector memory (EM) or terminally differentiated effectors re-expressing CD45RA (TEMRA) cells from both $CD4^+$ and $CD8^+$ subpopulations. In unstimulated samples, significant increases were detected within three clusters corresponding to $CD8^+$ and DN T-cell subsets (Supp. Figure 4.B), whereas increases were detected in one $CD4^+$ and one $CD8^+$ cluster in TB2-

stimulated samples (Supp. Figure 4.C) and only in $CD4^+$ clusters in rmsHBHA samples (Supp. Figure 4.D). Clusters that decreased between T0 and T1 (Supp. Figure 4.E)were detected only within $CD8^+$ EM and TEMRA cells in all stimulation conditions (Supp. Figure 4.F to 4.H).

Between T0 and T2, 11 increased clusters were detected (Figure 3.A). They corresponded mostly (8/11 clusters, 73%) to $CD4^+$ EM and CM subpopulations rather than naïve subsets, regardless of the stimulation condition (Figure 3.B. to 3.D.). One DN cluster was increased in unstimulated samples (Figure 3.B. as well as one $CD8^+$ TEMRA cluster and one γδ T-cell cluster in rmsHBHA stimulated samples (Figure 3.D.). One $CD4^+$ CM cluster (number 38) increased significantly in samples from all three stimulation conditions. Clusters which decreased between T0 and T2 were detected in one $CD8^+$ EM and two $CD8^+$ TEMRA subsets, and in seven clusters within $CD4^+$ subpopulations in all three stimulation conditions (Figure 3.E to 3.H). Regarding the latter clusters, no clear trend was observed regarding memory subset compartmentalization, which suggests that the abundance decrease spared memory functions and rather affected $CD4^+$ T-cells in general. One γδ and one DN T-cell cluster also decreased significantly within *Mtb*-stimulated samples (Figure 3.G. and 3.H.).

Antigen-driven cluster abundance changes during TB treatment show involvement of effector and memory T-cells.

To further refine patterns in functional marker expressions within increased or decreased clusters, we then performed a detailed phenotype analysis using marker expression heatmaps and hierarchical clustering (Figure 4). Four subgroups of cellular subsets of similar abundance changes and similar immunophenotypes were identified (labeled from A to D). Subgroup A included four $CD4^+$ T-cell clusters with naive (n=2) and CM (n=2) phenotypes, which decreased from T0 to T2 in rmsHBHA-stimulated samples. Subgroup B included five $CD8^+$ T-cell clusters that decreased throughout treatment, two of them between T0 and T1 and three of

193 them between T0 and T2. Consistently with the above results (Figure 3.E.), the latter were either
194 EM or TEMRA cells, with low CD45RA levels and intermediate levels of perforin. The other
195 two clusters were naïve clusters with low CCR7, CD45RA, and CD27 expression levels.
196
197 In contrast, subgroup C and D included only $CD4^+$ T-cell clusters, most of which (70%, 7/10)
198 increased between T0 and T2. Subgroup C consisted in five clusters exhibiting a CM phenotype
199 and expressing activation markers, detected in unstimulated and TB2-stimulated samples.
200 Subgroup D clusters were detected in *Mtb*-stimulated samples (3 in rmsHBHA and 2 in TB2)
201 and had an EM phenotype, except for cluster 69 that had a CM phenotype with low levels of
202 CCR7. These clusters co-expressed CD26, IL7Ra, CD7 and CD27. They were characterized by
203 an absence of activation marker expression and an enhanced expression of exhaustion markers,
204 in particular CTLA-4 and PD-1. Overall, we observed antigen-driven T-cell subset abundance
205 changes between T0 and T2. In TB2 and rmsHBHA samples, $CD4^+$ EM clusters mostly
206 increased, while $CD8^+$ EM clusters mostly decreased.
207
208 **Individual profiling confirms abundance changes in phenotypically homogeneous,**
209 **correlated subsets after treatment in cured patients.**
210 As the differentially abundant clusters identified above accounted for a small fraction of $CD3^+$
211 T-cells (<1%), we intended to identify the largest possible subsets of phenotypically
212 homogeneous cells within which a significant abundance change was detectable (Figure 5).
213 Within the subgroups of similar immunophenotypes and abundance change identified in
214 Figures 3 and 4, we performed correlation analyses at baseline and pooled the best correlated
215 clusters together within the subgroups identified in Figure 4 (Figure 5.A and 5.D). We then
216 visualized the individual abundance change of these pooled subsets before and after treatment
217 completion in cured patients (Figure 5.B-C and 5.D-E). Within rmsHBHA samples, a decrease

in subgroup A and an increase in subgroup D were both detected in 93% (13/14) of cured participants (Table 1). Within unstimulated samples, a decrease in subgroup B and an increase in subgroup C were recorded in 81% (13/16) and 88% (14/16) of patients respectively. This confirmed that the median trends observed previously were maintained individually in most patients. Finally, we visualized the immunophenotypes of these four subgroups of interest in comparison to cells from similar subpopulations which were not associated to cure (Figure 5.F). Subgroup A and subgroup C corresponded to $CD4^+$ CM cells expressing CCR6, IL7Ra, CD27, and activation markers (CD40L, CD38). However, cells within subgroup A expressed HLA-DR while subgroup C did not; in addition, cells from subgroup C expressed high levels of CD26, as well as CCR4, CXCR3, and CD7. Subgroup B corresponded to $CD8^+$ $CD7^+$ $Perforin^+$ EM cells. Subgroup D corresponded $CD4^+$ EM cells expressing high levels of CD26, as well as CCR4, CCR6, CXCR3, IL7Ra, CD7, and CD27. We then confirmed these findings by manually gating the identified subpopulations and comparing the percentages at T0 and T2 (Figure 5.G-K, representative dot plots).

Patients with persistent positive cultures at T1 show decreased peripheral $CD8^+$ cytotoxic subsets and enriched peripheral $CD4^+$ naïve subsets throughout treatment compared to patients with negative cultures at T1.

Then, we aimed to detect a cellular signature associated with mycobacterial conversion. To do so, we analyzed individual cluster abundance in slow *vs*. fast converters throughout treatment. At T0, T1, and T2, respectively 21, 24, and 21 clusters with significantly different abundance in slow converters compared to fast converters were detected (quantification in Supp. Fig. 5). After phenotyping, the proportions of the main T-cell subpopulation phenotypes in each group of enriched or decreased clusters at T0, T1, and T2 were calculated and summarized in Table 2.

Before treatment initiation, of 21 clusters with different abundance, 18 (86%) were decreased (Supp. Figure 5.A) and three (14%) were enriched (Supp. Figure 5.B) in slow compared to fast converters. Clusters which were under-represented in slow converters corresponded mostly to DN, γδ, and $CD8^+$ T-cells (77%, 13/18 clusters), specifically γδ and $CD8^+$ EM T-cell subpopulations (38%, 5/13 each); in addition, a majority of these clusters was $perforin^+$ (67%, 12/18) (Supp. Figure 6.A). In contrast, the three enriched clusters were naive $CD4^+$ and $CD8^+$ T-cells, as well as one $CD8^+$ TEMRA subset.

At T1, of 24 clusters with significantly different abundance between slow and fast converters, 15 (62%) were decreased (Figure 6.A and 6.C) and 9 (38%) were enriched in slow converters (Figure 6.B and 6.D). These clusters were mostly detected in TB2-stimulated samples (63%; 15/24 clusters). Comparison to the reference UMAP (Figure 6.E) and hierarchical clustering (Figure 6.F) indicated that enriched and decreased subsets respectively had similar immunophenotypes. Clusters which were under-represented at T1 in slow converters were mostly $perforin^+$ cells (67%, 10/15 clusters); mostly $CD8^+$ TEMRA and DN T-cell phenotypes were represented (40%, 6/15 clusters respectively). In contrast, enriched clusters comprised a majority of $CD4^+$ T-cells (78%, 7/9 clusters), with predominantly naïve phenotypes (45%, 3/7). One $CD8^+$ naive and one $CD8^+$ EM cluster were also enriched in slow converters at T1, with the latter expressing ICOS.

After treatment completion, of 21 clusters with significantly different abundance between slow and fast converters, 11 (52%) were decreased (Supp. Figure 5.C) and 10 (48%) were enriched in slow converters (Supp. Figure 5.D). The immunophenotype profile at T2 was similar to that of T1 for the enriched subsets: a majority of $ICOS^+$ $CD4^+$ naïve T-cell subsets (50%, 5/10) were detected, as well as two $CD8^+$ naïve clusters (Supp. Figure 6.B). Regarding the decreased subsets, no specific phenotype polarization was observed, and clusters were detected within diverse subsets (four $CD8^+$ EM clusters, four $CD4^+$ EM clusters, and three DN T-cells clusters).

Similarly to the T1 immune profile, all of the above clusters were mostly detected in TB2-stimulated samples (67%, 14/21 clusters).

Maturation markers and chemokine receptors, rather than activation or cytotoxic markers, discriminate slow from fast converters during treatment.

Finally, we sought to assess more precisely which combinations of cellular markers were the most involved in the discrimination between fast and slow converters within the clusters identified in the prior section. A principal component analysis (PCA) was performed on marker expression data within these clusters. As a higher number of differentially abundant clusters had been detected in *Mtb*-stimulated samples than in unstimulated samples during treatment (T1 and T2), and because a complete overlap between the PCA profiles of fast and slow converters was observed in unstimulated samples, we focused on *Mtb*-stimulated samples (TB2 and rmsHBHA). PCA profiles were mostly separated when split by culture conversion group (Figure 7.a). Dimension 1 (Dim1) explained 37.3% of the total observed variance, versus 12.5% for Dim2. The main markers accounting for variance described by Dim1 were markers of memory subset definition (CCR7 and CD45RA), lineage (CD4 and TCRγδ), maturation (CD27 and CD7), chemokine receptors (CCR4 and to a lesser extent CXCR3) or other receptors or costimulatory molecules (*e.g.*, CD26, CD161) (Figure 7.B. and 7.C). In contrast, variance described by Dim2 was mostly explained by cytotoxicity (Perforin, CD56, CD8), activation (CD38, CD40L, CD69), or exhaustion markers (CD152, PD-1) (Figure 7.B and 7.D). The PCA scores were significantly higher in slow converters than in fast converters at all timepoints for Dim1 (Figure 7.E), indicating that the immune profile of slow converters was more correlated to Dim1 than that of fast converters regardless of the timepoint. In contrast, no significant differences were detected at the end of treatment (T2) for Dim2 (Figure 7.F). When comparing these results with PCA analyses performed on total $CD3^+$ T-cells, fast and slow converter

292 profiles were less separated, but similar marker involvement was observed in Dim1 and Dim2

293 respectively (Supp. Figure 7).

Discussion

In a population of adults treated for TB, we observed a shift towards more differentiated profiles among peripheral $CD8^+$ and $CD4^+$ T-cell subsets driven by the timing of *Mtb* culture conversion, using a high-dimensional single cell approach after stimulation with standardized, IVD-level TB2 antigens. In particular, differentiated $CD8^+$ cytotoxic effector subsets were under-represented in positive- versus negative-sputum culture patients after two months of treatment.

Over the course of TB treatment, we observed as a general trend that non-canonical subsets within CM $CD4^+$ and TEMRA $CD8^+$ populations increased, whereas naïve $CD4^+$ and naïve/EM $CD8^+$ subsets decreased. This is consistent with prior works addressing T-cell differentiation and T-cell memory subsets during TB treatment (Marriott et al., 2018; Chiacchio et al., 2014; Wang et al., 2010). *Mtb*-specific $CD4^+$ EM T-cells have been associated with active TB disease, whereas CM T-cells have been associated to latency and increased upon treatment (Petruccioli et al., 2013; Goletti et al., 2006a). In *Mtb*-specific $CD8^+$ T-cells, an overall decrease in peripheral blood (Nyendak et al., 2013) and a decrease in CM cells (Axelsson-Robertson et al., 2015b) have been documented after treatment. In contrast, the central result of this study was to distinguish negative- from positive-sputum culture patients at two months, whether infected with a DS- or DR-*Mtb* strain, through differential peripheral T-cell populations. When retrospectively analyzing the T-cell profiles of fast and slow converters at diagnosis, a pre-existing difference in percentages of cytotoxic EM $CD8^+$ T-cell subpopulations was already observed. After two months of treatment, this trend shifted into an under-representation of $CD8^+$ TEMRA, which persisted after cure. These changes were revealed upon stimulation with QFT-P TB2 antigenic peptide pools. Although many studies characterizing T-cell subsets during treatment have clearly underlined the importance of *Mtb*-specific $CD4^+$ T-cells (Riou et al., 2014; Ahmed et al., 2018b; Riou et al., 2020), less is known about the role of $CD8^+$ T-cells

in TB resolution and the most appropriate epitopes to study them in this context (Lewinsohn et al., 2017; Chiacchio et al., 2018). Yet, effector $CD8^+$ T-cells are known to secrete cytolytic and antimicrobial factors that kill *Mtb*-infected macrophages *in vitro* (Serbina et al., 2000), inhibit *Mtb* growth (Lewinsohn et al., 2017), and are required for long-term infection control in mice (Lin and Flynn, 2015) and humans (Bruns et al., 2009); perforin production by $CD8^+$ T-cells is also higher in treated than in untreated TB patients (Jiang et al., 2017). In addition, a 2012 study by Rozot and colleagues had associated *Mtb*-specific TEMRA $CD8^+$ T cells to LTBI and EM cells to active TB (Rozot et al., 2013). Here, although we cannot establish causality, a lower peripheral $CD8^+$ TEMRA subset abundance may be associated with slower mycobacterial culture conversion. In relation with abundance changes during treatment, our study hints that the $CD8^+$ T-cell phenotype shift occurring during TB treatment would be delayed in patients with slower microbiological conversion. Consistently, it has been shown that $CD8^+$ response importantly contributed to the control of other granulomatous infections such as *Brucella* (Durward et al., 2012). Regarding $CD4^+$ T-cells, naïve subsets were over-represented in slow converters, which suggests a delayed differentiation within the $CD4^+$ compartment as well. Previous work has shown that the IFN-γ/IL-2/TNF-α functional profile of *Mtb*-specific $CD4^+$ T-cells, which is key in anti-TB immunity (Chiacchio et al., 2017), was correlated with their degree of differentiation (Riou et al., 2017). Taken together, these results support the hypothesis that $CD4^+$ and $CD8^+$ T-cell responses should be monitored together during TB treatment, as successful mycobacterial clearance involves $CD8^+$ T-cell effectors, which in turn require $CD4^+$ T-cell involvement (Grotzke and Lewinsohn, 2005).

Although the aim of this study was not to compare stimulation conditions, but to use them to uncover cell clusters, our results suggest that the abundance changes observed throughout treatment are antigen-driven. This adds to previous work highlighting differential *Mtb*-specific $CD8^+$ T-cells marker profiles according to the nature of the antigen stimulation (Axelsson-

Robertson et al., 2015a). We used QFT-P TB2, which elicits cytotoxic $CD8^+$ responses in addition to ESAT-6/CFP-10-induced $CD4^+$ responses (Petruccioli et al., 2016), as well as rmsHBHA, a recombinant *Mtb* protein exposing many different epitopes. The latter was included because the IFN-γ response to HBHA, to which both $CD4^+$ and $CD8^+$ cells participate (Masungi et al., 2002), is impaired in active TB patients and restored during treatment (Chedid et al., 2021; Sali et al., 2018; De Maio et al., 2018). Here, changes during treatment in $CD8^+$, $CD4^+$, DN, and γδ T-cell subsets were detectable within unstimulated and TB2 samples, consistently with previous works (Petruccioli et al., 2016). In contrast, in rmsHBHA-stimulated samples, significant abundance changes were mostly detected within $CD4^+$ T-cells, suggesting a preferential $CD4^+$ T-cell response to HBHA epitopes during treatment. This indicates that antigen-driven changes during the response to *Mtb* are part of a complex process involving a variety of different epitopes (Axelsson-Robertson et al., 2015b) that induce responses from phenotypically diverse T-cell subsets (Axelsson-Robertson et al., 2015a), despite well-described immunodominance features. Our results confirm that a major stake in discovering blood-based immune signatures of mycobacterial sterilization lies in finding the appropriate epitopes.

Finally, our study enabled profiling of non-lineage markers. A $CXCR3^+$ $CCR6^+$ $CD27^+$ $CD4^+$ EM subset was increased in cured patients compared to pre-treatment, corresponding to a subset enriched in Th1/Th17 cells (Kim et al., 2001; Acosta-Rodriguez et al., 2007). Consistently with previous work on LTBI (Lindestam Arlehamn et al., 2013), this suggests that an increase in these cells upon cure might be associated with infection control. Compared to the other $CD4^+$ EM cells, this subset displayed higher CD26 and IL7Ra expression. CD26 participates in T-cell activation and proliferation (Klemann et al., 2016), and correlates with Th1-like responses (Ohnuma et al., 2008). In parallel, a significant decrease was also observed in a highly activated $CCR6^+$ $IL7Ra^+$ $CD4^+$ CM subset, which expressed higher levels of CD40L, CD38, and HLA-

DR than other $CD4^+$ CM cells. Interestingly, an increase in another $CD4^+$ CM subset – which differed from the latter because it expressed CD26 and CD27, but not HLA-DR – was observed simultaneously. This adds to previous works highlighting a decrease in $CD38^+$ and $HLA\text{-}DR^+$ *Mtb*-specific $CD4^+$ T-cells in successfully treated TB patients (Ahmed et al., 2018a; Riou et al., 2020; Adekambi et al., 2015b). This suggests that upon TB treatment, differentiated Th1/Th17-like $CD4^+$ subsets expressing high levels of CD26 and IL7Ra are enriched in peripheral blood, likely at the expense of less differentiated subsets expressing high levels of CD27 and CD38. Finally, principal components analysis showed that within the subpopulations that differentiated slow from fast converters during treatment, differentiation markers and chemokine receptors contributed to most of the variance, followed by activation and cytotoxicity markers. CD27, CD26, and CCR4 were among the markers which best discriminated fast and slow responders, consistently with prior studies associating CD27 and CCR4 expression in *Mtb*-specific $CD4^+$ T-cells with active TB compared to latent infection (Latorre et al., 2019). HLA-DR and CD38 also contributed to a lesser extent, which adds to a recent study in which co-expression of CD27, HLA-DR, and CD38 on PPD-stimulated $CD4^+$ T-cells stratified fast and slow responders without restriction to IFN-γ-producing cells (Vickers et al., 2020).

This descriptive study has limitations. The number of patients included was low, resulting in few slow converters, consistently with treated TB course (15 to 20% of slow culture converters). In addition, the presence of within-host *Mtb* isolate micro-diversity has been recently proven in patients treated for DS-TB without culture conversion after two months of well-conducted TB treatment (Genestet et al., 2021), suggesting that it could modulate the host response. We are currently conducting a larger validation study including DS-TB patients only, from whom *Mtb* isolates collected upon treatment initiation and at two months will be screened by whole genome sequencing. In addition, the analyses were not conducted on live cells, but on fixed,

cryopreserved peripheral blood cells due to the design of the study using samples collected in lower-income, high TB prevalence settings. For the same reason, the study was conducted on peripheral blood, while the main infectious focus of TB is in the lungs. In addition, since the study required to IGRAs to be performed on the same blood samples prior to cell cryopreservation (Chedid et al., 2021), we did not perform intracellular cytokine staining. Hence, the integrality of the observed cell phenotype changes may not be associated with *Mtb*-specific responses. However, whether the bulk of anti-TB response relies purely on *Mtb*-specific cells is debated. Given the complexity of the immune response to TB, cellular and molecular interactions are likely to occur between *Mtb*-specific and non-specific subpopulations during mycobacterial clearance, and hence influence the overall T-cell profiles. In addition, the hypothesis that T-cells specific for immunodominant epitopes actually recognize *Mtb*-infected cells has been challenged by studies on mouse models (Patankar et al., 2020), protective immunity post-BCG vaccination(Kagina et al., 2010), and failures of vaccine candidates based on immunodominant antigens (Moguche et al., 2017).

These limitations are linked to the "bench to bedside" approach adopted in our study. They reflect the reality of the needs for novel TB management tools: accessible samples, simple experimental process, straightforward output. Here, we captured the complexity of T-cell profiles during treatment and narrowed it down to subpopulations of interest associated with cure at the individual level. Although mass cytometry requires complex equipment, experiments, and analyses, we have shown that relevant T-cell profiles could be identified in cryopreserved samples, obtained from small blood volumes, using manual gating analyses and a smaller number of core markers. Future validation studies might confirm the relevancy of simpler phenotypic signatures translatable in primary care settings. Importantly, our study revealed T-cell populations discriminating patient status based on culture conversion, which has a dual impact: on TB management, to better characterize the phenotypes of T-cells involved

419 in TB clearance; and on biomarker research, further supporting that a diversity of epitopes is
420 needed to fully disclose the spectrum of these cells. This work may help identify simpler
421 prognostic biomarkers associated with mycobacterial clearance and the antigens appropriate for
422 their discovery.
423

Materials and methods

Experimental design

Study design and research objectives

This prospective cohort study was nested in a multicentered study coordinated by the Mérieux Foundation GABRIEL network (Chedid et al., 2020). The primary objective was to investigate the association between sputum culture sterilization during TB treatment and T-cell profiles obtained by high-dimensional phenotyping. The sample size was maximized based on availability of clinical samples. No prospective sample size calculations were performed.

Recruitment centers and ethical considerations

Recruitment centers were the National Center for Tuberculosis and Lung Disease (NTCLD) in Tbilisi, Georgia (approval of the Institutional Review Board of the NTCLD; IORG0009467); and the International Centre for Diarrhoeal Disease Research, Bangladesh (icddr,b) in Dhaka, Bangladesh (approval of the Research Review Committee and the Ethical Review Committee of icddr,b; PR-17076; Version No. 1.3; Version date: 04-01-2018). All participants provided written informed consent.

Cohort recruitment, patient follow-up, and clinical data collection

Patients were recruited if diagnosed with sputum culture confirmed pulmonary TB and older than 15 years old. Patients with HIV, immune deficiency, diabetes mellitus, and lost-to-follow-up were excluded. Detailed procedures for microbiological diagnosis, drug susceptibility testing, and treatment regimens are described elsewhere (Chedid et al., 2020). As antimicrobial resistance is a major challenge for TB management and treatment, both drug-susceptible (DS-TB) and drug-resistant (DR-TB) patients were recruited to examine immune profiles in these settings. Patients were followed up: at inclusion (T0), after two months of treatment (T1), and at the end of TB treatment (T2; 6 months for DS-TB patients, 9 to 24 months for DR-TB patients). The T1 timepoint was chosen because it marks the moment after which antibiotic

449 treatment is reduced during clinical DS-TB management. For DR-TB monitoring, the same
450 timepoint was used for consistency. Patients were on Directly Observed Treatment (DOT) and
451 received treatment according to standard protocols (World Health Organization Geneva, 2019).
452 Treatment regimens are detailed in Supp. Table 1.
453
454 **Whole blood stimulation and processing**
455 Detailed whole blood collection and stimulation processes were described elsewhere (Chedid
456 et al., 2021). Briefly, at every follow-up visit, 1mL of whole blood was drawn from the
457 antecubital area of the arm and seeded directly into each QuantiFERON-TB Gold Plus (QFT-
458 P, Qiagen) tube and incubated for 24 hours. Three stimulation conditions were used: NIL as
459 unstimulated control; TB2 which tubes contain the *M. tuberculosis* antigenic peptides ESAT-6
460 (>15aa) and CFP-10 (8-13aa), which induce responses from $CD4^+$ T lymphocytes (Petruccioli
461 et al., 2016), and an undisclosed peptide pool inducing $CD8^+$ T lymphocyte stimulation
462 (Qiagen, 2017); rmsHBHA which tubes contain recombinant *M. tuberculosis* heparin-binding
463 hemagglutinin generated in *M. smegmatis* at a final concentration of 5µg/mL and graciously
464 provided by the Delogu laboratory, UNICATT, Rome, Italy (Delogu et al., 2011). After
465 incubation, plasma separation, and red blood cell lysis with FACS lysing buffer (BD
466 Biosciences) according to the manufacturer's instructions, the resulting fixed white blood cells
467 pellets were stored at -80°C. Cryopreserved samples were air-shipped in dry ice with freezing
468 controls to the Mérieux Foundation Emerging Pathogens Laboratory in Lyon, France
469 (International Center for Infectiology Research, INSERM U1111).
470

Experimental procedure for mass cytometry

Sample preparation

Cryopreserved cells were thawed and resuspended in phosphate buffer saline (PBS) to a concentration of $3.5x10^6$cells/mL. Between 1 and $1.5x10^6$ cells from each sample were aliquoted for staining. Cells were incubated 10 minutes with FcR Blocking Reagent (6µL/10^6 cells; Miltenyi Biotec) and heparin sodium salt reconstituted in Millipore water (36µg/10^6 cells; Sigma-Aldrich) to reduce nonspecific staining (Rahman et al., 2016).

Panel design

A 29-marker panel of metal-labeled antibodies was used. All antibodies were obtained from Fluidigm (Supp. Table 8). Briefly, the panel contained 28 T-cell oriented surface markers (lineage markers, chemokine receptors, activation markers, and exhaustion markers) and one intracellular target (perforin).

Experimental design and barcoding

As the study followed a longitudinal design, samples from a same patient were acquired in the same barcoded batch of 3 timepoints and 3 stimulation conditions to reduce experimental variation. Palladium barcoding (Mei et al., 2015) (Cell-ID 20-Plex, Fluidigm) was performed according to the manufacturer's instructions for simultaneous staining and data acquisition. For each barcoding run, 18 patient T-cell samples were stained with unique combinations of intracellular palladium isotopes (Figure 1). Patient batches were processed in a random order and investigators were blinded to patient sputum culture results during data collection.

Staining procedure

Extracellular staining was performed on pooled barcoded cells in Maxpar cell staining buffer (Fluidigm) for 30 minutes at room temperature. Intracellular staining (perforin) was performed in Maxpar Perm-S Buffer (Fluidigm) for 30 minutes at room temperature. Stained cells were then incubated for 10 minutes in 1.6% formaldehyde (FA) freshly prepared from 16% stock FA

(Sigma-Aldrich). DNA staining was performed by overnight incubation at 4°C in 2mL of 125nM Cell-ID Iridium intercalator solution (Fluidigm). Cells were then washed, pelleted, and kept at 4°C until acquisition.

Data acquisition

Samples were analyzed on a CyTOF2 mass cytometer upgraded to Helios (Fluidigm) hosted by the AniRA cytometry facility (Structure Fédérative de Recherche Lyon Gerland, INSERM U1111, Lyon, France). Samples were filtered twice through a 50µm nylon mesh and resuspended in EQ™ Four Element Calibration Beads (Fluidigm) diluted to 0.5X in Maxpar ultra-pure water (Fluidigm), to reach an acquisition rate of 150-200 events per second (0.5 x 10^6 cells/mL). Data were collected using the on-board Fluidigm software.

Data analysis

All data analyses were performed in RStudio (version 1.3.1073 with R version 4.0.3) and FlowJo (version 10.7.1).

Data cleaning and preliminary manual gating

Signal normalization, concatenation, debarcoding, and conversion into Flow Cytometry Standard (FCS) 3.0 format were performed using the Helios Software (Fluidigm). Debarcoded files were imported into FlowJo and arcsinh-transformed (cofactor = 5). Gaussian parameters of the Helios system were used for doublet exclusion (Leipold et al., 2015), then $^{191}Ir^+$ $^{193}Ir^+$ single events were manually isolated, and debris ($CD45^-$ events) and calibration beads ($^{140}Ce^+$ events) were excluded). A preliminary manual gating analysis was then performed on $CD45^+$ single events (Supp. Figure 8) to verify that the proportions of the main white blood cell subpopulations in biobanked samples were consistent with the expected proportions, and sufficient for downstream analysis. Samples with less than 1,000 $CD3^+$ events, and batches with missing samples from a given timepoint were removed from the analysis to preserve a matched

sample design. The exact number of available files per patient and per stimulation condition is provided in Supp. Table 1.

Workflow for unsupervised analyses

$CD3^+$ single events were down-sampled to ensure equal contribution of each sample, exported into separate Comma Separated Value (.csv) files, and uploaded into R software (version 4.0.3). Panel markers were defined as either lineage or functional markers for use as clustering channels in downstream analyses (Supp. Table 9). Lineage-defining markers included canonical surface markers such as CD4 which display a theoretically stable expression. Functional markers included markers of activation (*e.g.* CD69), proliferation (CD38), maturation (CD27), or migration (CCR7).

Dimension reduction, automated clustering, and phenotyping

After file concatenation, dimension reduction was performed with UMAP (Uniform Manifold Approximation and Projection; version 3.1) (Becht et al., 2019). UMAPs were created in R using the package Spectre (Ashhurst et al., 2020). Unsupervised clustering was performed using FlowSOM (Van Gassen et al., 2015) (version 2.7). FlowSOM meta-cluster phenotyping was assessed by visualizing the surface expression of lineage markers in each FlowSOM cluster (CD4, CD8, TCRgd, TCRVa7.2, CD56, CD25, IL7Ra, CD26, and CD161) on a heatmap and performing hierarchical clustering. Marker expression heatmaps were obtained in R using Spectre by plotting normalized, median arcsinh-transformed mass signals. Biological consistency of FlowSOM meta-clusters with the main expected T-cell subpopulations (Supp. Table 3) was controlled, and manual reassignment of clusters which were in inconsistent meta-clusters was then performed when necessary (Supp. Figure 9). Meta-clusters with an abundance <1% of all events were pooled with the most phenotypically similar meta-cluster. Then, the proportion of corrected FlowSOM meta-clusters in each node on the initial FlowSOM minimum spanning tree was visualized to control reassignment consistency (Quintelier et al., 2021).

Statistical analysis

The proportion (percent of $CD3^+$) of each FlowSOM cluster was calculated. For all statistical analyses, exact p-values, test statistics and/or estimates of effect size are provided either in the figure legend or in indicated Supplementary Tables. Normality was assessed using the Shapiro-Wilk test. The evolution of cluster proportions over time corresponded to repeated measures of non-normal, non-independent continuous variables, and was analyzed in matched samples using the two-sided Friedman rank sum test with the Wilcoxon–Nemenyi–McDonald-Thompson post-hoc test (Pereira et al., 2015). Independent, non-normal continuous variables were analyzed with the two-sided Mann–Whitney U test or the Kruskal–Wallis test with Dunn's Kruskal–Wallis Multiple Comparisons *post-hoc* test (Dunn, 1964) when more than two categories were compared. For discovery of clusters with significantly different abundance between slow and fast converters, conservative corrections for multiple comparisons (*e.g.* Benjamini-Hochberg (Yoav Benjamini and Yosef Hochberg, 1995)) were not used in order to minimize type II errors. Instead, all p-values were computed for each timepoint, and the p-value corresponding to the null hypothesis being rejected in 5% of all comparisons was used as the significance threshold instead of 0.05 (Althouse, 2016). This novel significance threshold enabled to control type I error while maintaining an exploratory approach; its value was always inferior to 0.05 and is reported in the corresponding figure captions.

Supplemental Materials

Supp. Figure 1 is a flowchart of patient inclusions. Supp. Figure. 2 shows the impact of *in vitro Mtb* antigen whole blood stimulation on surface marker expression in the main T-cell compartments. Supp. Figure. 3 summarizes the frequencies of the main peripheral T-cell subpopulations throughout anti-TB treatment. Supp. Figures 4 to 6 quantify and illustrate how patients with slow microbiological culture conversion show decreased $CD8^+$ and enriched

571 $CD4^+$ naïve peripheral T-cell subsets during treatment. Supp. Figure 7 reports PCA data
572 characterizing the variance between fast and slow responders within all *Mtb*-stimulated $CD3^+$
573 T-cells. Supp. Figure 8 and 9 relate to the Methods section, and show the main $CD45^+$ non-
574 granulocyte whole blood subpopulations, a T-cell oriented gating strategy, as well as the
575 methods used to control automated FlowSOM metaclustering. Regarding tables, Supp. Table 1
576 summarizes the sociodemographic and clinical characteristics of the cohort. Supp. Tables 2
577 through 7 list the exact p-values and test statistics for all analyses presented throughout the main
578 manuscript. Supp. Table 8 lists the mass cytometry panel components. Supp. Table 9 shows
579 how clustering channels were defined in relation to expected cell subpopulations for dimension
580 reduction and automated clustering of $CD3^+$ T-cells.
581

582 ## Author contributions

583 FA and JH are the principal investigators and initiated the project together with DG, NT, and
584 SBa. Samples were collected by EK, NT, MU, and SBi. CC and TA designed and optimized
585 the mass cytometry protocol. CC performed all experiments and analyses. CC and FA wrote
586 the manuscript. All authors contributed to the article and approved the submitted version.
587

588 ## Acknowledgements

589 We would like to thank the patients participating in our study, as well as the healthcare staff
590 and laboratory collaborators in each study site.
591

592 **Funding**

593 This work was supported by Fondation Mérieux, Fondation Christophe et Rodolphe Mérieux,
594 and Fondation AnBer, and the grant ANR-18-CE17-0020. A minor part of the study was
595 supported by the Italian Ministry of Health "Ricerca Corrente, Linea 4."

596

597 **Competing Interests**

598 DG reports personal fees from Biomérieux (consulting), Qiagen (consulting, lectures), and
599 Diasorin (lectures) outside the submitted work. The authors declare no other competing
600 interests.

601

602 **Data availability**

603 The datasets generated and used in this study are available from the corresponding author
604 upon reasonable request, excluding confidential patient information.

605

606

References

Acosta-Rodriguez, E. V., L. Rivino, J. Geginat, D. Jarrossay, M. Gattorno, A. Lanzavecchia, F. Sallusto, and G. Napolitani. 2007. Surface phenotype and antigenic specificity of human interleukin 17-producing T helper memory cells. *Nat. Immunol.* 8:639–646. doi:10.1038/ni1467.

Adekambi, T., C.C. Ibegbu, S. Cagle, A.S. Kalokhe, Y.F. Wang, Y. Hu, C.L. Day, S.M. Ray, and J. Rengarajan. 2015a. Biomarkers on patient T cells diagnose active tuberculosis and monitor treatment response (vol 125, pg 1827, 2015). *J. Clin. Invest.* 125:3723. doi:10.1172/jci83279.

Adekambi, T., C.C. Ibegbu, S. Cagle, A.S. Kalokhe, Y.F. Wang, Y. Hu, C.L. Day, S.M. Ray, and J. Rengarajan. 2015b. Biomarkers on patient T cells diagnose active tuberculosis and monitor treatment response. *J. Clin. Invest.* 125:1827–1838. doi:10.1172/jci77990.

Agrawal, S., O. Parkash, A.N. Palaniappan, A.K. Bhatia, S. Kumar, D.S. Chauhan, and M. Madhan Kumar. 2018. Efficacy of T regulatory cells, Th17 cells and the associated markers in monitoring tuberculosis treatment response. *Front. Immunol.* 9:1–16. doi:10.3389/fimmu.2018.00157.

Ahmed, M.I.M., N.E. Ntinginya, G. Kibiki, B.A. Mtafya, H. Semvua, S. Mpagama, C. Mtabho, E. Saathoff, K. Held, R. Loose, I. Kroidl, M. Chachage, U. von Both, A. Haule, A.M. Mekota, M.J. Boeree, S.H. Gillespie, M. Hoelscher, N. Heinrich, and C. Geldmacher. 2018a. Phenotypic Changes on Mycobacterium Tuberculosis-Specific CD4 T Cells as Surrogate Markers for Tuberculosis Treatment Efficacy. *Front. Immunol.* 9:2247. doi:10.3389/fimmu.2018.02247.

Ahmed, M.I.M., N.E. Ntinginya, G. Kibiki, B.A. Mtafya, H. Semvua, S. Mpagama, C. Mtabho, E. Saathoff, K. Held, R. Loose, I. Kroidl, M. Chachage, U. von Both, A. Haule, A.M. Mekota, M.J. Boeree, S.H. Gillespie, M. Hoelscher, N. Heinrich, C. Geldmacher,

and E. Pan African Consortium. 2018b. Phenotypic Changes on Mycobacterium Tuberculosis-Specific CD4 T Cells as Surrogate Markers for Tuberculosis Treatment Efficacy. *Front. Immunol.* 9:13. doi:10.3389/fimmu.2018.02247.

Althouse, A.D. 2016. Adjust for Multiple Comparisons? It's Not That Simple. *Ann. Thorac. Surg.* 101:1644–1645. doi:10.1016/j.athoracsur.2015.11.024.

Ashhurst, T.M., F. Marsh-Wakefield, G.H. Putri, A.G. Spiteri, D. Shinko, M.N. Read, A.L. Smith, and N.J.C. King. 2020. Integration, exploration, and analysis of high-dimensional single-cell cytometry data using Spectre. *bioRxiv*. doi:10.1101/2020.10.22.349563.

Axelsson-Robertson, R., J.H. Ju, H.Y. Kim, A. Zumla, and M. Maeurer. 2015a. Mycobacterium tuberculosis-specific and MHC class I-restricted CD8+ T-cells exhibit a stem cell precursor-like phenotype in patients with active pulmonary tuberculosis. *Int. J. Infect. Dis.* 32:13–22. doi:10.1016/j.ijid.2014.12.017.

Axelsson-Robertson, R., M. Rao, A.G. Loxton, G. Walzl, M. Bates, A. Zumla, and M. Maeurer. 2015b. Frequency of Mycobacterium tuberculosis-specific CD8+ T-cells in the course of anti-tuberculosis treatment. *Int. J. Infect. Dis.* 32:23–29. doi:10.1016/j.ijid.2015.01.017.

Becht, E., L. McInnes, J. Healy, C.A. Dutertre, I.W.H. Kwok, L.G. Ng, F. Ginhoux, and E.W. Newell. 2019. Dimensionality reduction for visualizing single-cell data using UMAP. *Nat. Biotechnol.* 37:38–47. doi:10.1038/nbt.4314.

Bruns, H., C. Meinken, P. Schauenberg, G. Härter, P. Kern, R.L. Modlin, C. Antoni, and S. Stenger. 2009. Anti-TNF immunotherapy reduces CD8+ T cell–mediated antimicrobial activity against Mycobacterium tuberculosis in humans. *JCI*. 119:1167–1177. doi:10.1172/JCI38482.ated.

Chedid, C., E. Kokhreidze, N. Tukvadze, S. Banu, M.K.M. Uddin, S. Biswas, G. Russomando, C.C.D. Acosta, R. Arenas, P.P. Ranaivomanana, C. Razafimahatratra, P.

Herindrainy, J. Rakotonirina, A.H. Raherinandrasana, N. Rakotosamimanana, M. Hamze, M.B. Ismail, R. Bayaa, J.-L. Berland, F. De Maio, G. Delogu, H. Endtz, F. Ader, D. Goletti, and J. Hoffmann. 2021. Relevance of QuantiFERON-TB Gold Plus and Heparin-Binding Hemagglutinin Interferon-γ Release Assays for Monitoring of Pulmonary Tuberculosis Clearance: A Multicentered Study. *Front. Immunol.* 11:1–11. doi:10.3389/fimmu.2020.616450.

Chedid, C., E. Kokhreidze, N. Tukvadze, S. Banu, M.K.M. Uddin, S. Biswas, G. Russomando, C.C.D. Acosta, R. Arenas, P.P. Ranaivomanana, C. Razafimahatratra, P. Herindrainy, N. Rakotosamimanana, M. Hamze, M.B. Ismail, R. Bayaa, J.-L. Berland, G. Delogu, H. Endtz, F. Ader, D. Goletti, and J. Hoffmann. 2020. Association of baseline white blood cell counts with tuberculosis treatment outcome: a prospective multicentered cohort study. *Int. J. Infect. Dis.* doi:10.1016/j.ijid.2020.09.017.

Chiacchio, T., G. Delogu, V. Vanini, G. Cuzzi, F. De Maio, C. Pinnetti, A. Sampaolesi, A. Antinori, and D. Goletti. 2017. Immune characterization of the HBHA-specific response in mycobacterium tuberculosis-infected patients with or without HIV infection. *PLoS One*. 12:1–18. doi:10.1371/journal.pone.0183846.

Chiacchio, T., E. Petruccioli, V. Vanini, G. Cuzzi, M.P. La Manna, V. Orlando, C. Pinnetti, A. Sampaolesi, A. Antinori, N. Caccamo, and D. Goletti. 2018. Impact of antiretroviral and tuberculosis therapies on CD4+ and CD8+ HIV/M. tuberculosis-specific T-cell in co-infected subjects. *Immunol. Lett.* 198:33–43. doi:10.1016/j.imlet.2018.04.001.

Chiacchio, T., E. Petruccioli, V. Vanini, G. Cuzzi, C. Pinnetti, A. Sampaolesi, A. Antinori, E. Girardi, and D. Goletti. 2014. Polyfunctional T-cells and effector memory phenotype are associated with active TB in HIV-infected patients. *J. Infect.* 69:533–545. doi:10.1016/j.jinf.2014.06.009.

Delogu, G., T. Chiacchio, V. Vanini, O. Butera, G. Cuzzi, A. Bua, P. Molicotti, S. Zanetti,

F.N. Lauria, S. Grisetti, N. Magnavita, G. Fadda, E. Girardi, and D. Goletti. 2011. Methylated HBHA produced in M. smegmatis discriminates between active and non-active tuberculosis disease among RD1-responders. *PLoS One*. 6. doi:10.1371/journal.pone.0018315.

Dunn, O.J. 1964. Multiple Comparisons Using Rank Sums. *Technometrics*. 6:241–251. doi:10.1080/00401706.1965.10490253.

Durward, M., G. Radhakrishnan, J. Harms, C. Bareiss, D. Magnani, and G.A. Splitter. 2012. Active evasion of CTL mediated killing and low quality responding CD8+ T cells contribute to persistence of brucellosis. *PLoS One*. 7. doi:10.1371/journal.pone.0034925.

Van Gassen, S., B. Callebaut, M.J. Van Helden, B.N. Lambrecht, P. Demeester, T. Dhaene, and Y. Saeys. 2015. FlowSOM: Using self-organizing maps for visualization and interpretation of cytometry data. *Cytom. Part A*. 87:636–645. doi:10.1002/cyto.a.22625.

Genestet, C., E. Hodille, A. Barbry, J.-L. Berland, J. Hoffmann, E. Westeel, F. Bastian, M. Guichardant, S. Venner, G. Lina, C. Ginevra, F. Ader, S. Goutelle, and O. Dumitrescu. 2021. Rifampicin exposure reveals within-host Mycobacterium tuberculosis diversity in patients with delayed culture conversion. *PLOS Pathog.* 17:e1009643. doi:10.1371/journal.ppat.1009643.

Goletti, D., O. Butera, F. Bizzoni, R. Casetti, E. Giradi, and F. Poccia. 2006a. Region of difference 1 antigen-specific CD4+ memory T cells correlate with a favorable outcome of tuberculosis. *J. Infect. Dis.* 194:984–992. doi:10.1086/507427.

Goletti, D., O. Butera, F. Bizzoni, R. Casetti, E. Girardi, and F. Poccia. 2006b. Region of Difference 1 Antigen–Specific CD4 + Memory T Cells Correlate with a Favorable Outcome of Tuberculosis. *J. Infect. Dis.* 194:984–992. doi:10.1086/507427.

Goletti, D., C.S. Lindestam Arlehamn, T.J. Scriba, R. Anthony, D. Maria Cirillo, T. Alonzi, C.M. Denkinger, and F. Cobelens. 2018. Can we predict tuberculosis cure? Current tools

707 available. *Eur. Respir. J.* 1801089. doi:10.1183/13993003.01089-2018.

708 Gossez, M., T. Rimmelé, T. Andrieu, S. Debord, F. Bayle, C. Malcus, F. Poitevin-Later, and
709 G. Monneret. 2018. Proof of concept study of mass cytometry in septic shock patients
710 reveals novel immune alterations. *Sci. Rep.* 8:1–12. doi:10.1038/s41598-018-35932-0.

711 Grotzke, J.E., and D.M. Lewinsohn. 2005. Role of CD8+ T lymphocytes in control of
712 Mycobacterium tuberculosis infection. *Microbes Infect.* 7:776–788.
713 doi:10.1016/j.micinf.2005.03.001.

714 Horne, D.J., S.E. Royce, L. Gooze, M. Narita, P.C. Hopewell, P. Nahid, and K.R. Steingart.
715 2010. Sputum monitoring during tuberculosis treatment for predicting outcome :
716 systematic review and meta-analysis. *Lancet Infect. Dis.* 10:387–394.
717 doi:10.1016/S1473-3099(10)70071-2.

718 Jiang, H.B., H.L. Gong, Q. Zhang, J. Gu, L. Liang, and J. Zhang. 2017. Decreased expression
719 of perforin in CD8(+) T lymphocytes in patients with Mycobacterium tuberculosis
720 infection and its potential value as a marker for efficacy of treatment. *J. Thorac. Dis.*
721 9:1353-+. doi:10.21037/jtd.2017.05.74.

722 Kagina, B.M.N., B. Abel, T.J. Scriba, E.J. Hughes, A. Keyser, A. Soares, H. Gamieldien, M.
723 Sidibana, M. Hatherill, S. Gelderbloem, H. Mahomed, A. Hawkridge, G. Hussey, G.
724 Kaplan, and W.A. Hanekom. 2010. Specific T cell frequency and cytokine expression
725 profile do not correlate with protection against tuberculosis after bacillus Calmette-
726 Guérin vaccination of newborns. *Am. J. Respir. Crit. Care Med.* 182:1073–1079.
727 doi:10.1164/rccm.201003-0334OC.

728 Kim, C.H., L. Rott, E.J. Kunkel, M.C. Genovese, D.P. Andrew, L. Wu, and E.C. Butcher.
729 2001. Rules of chemokine receptor association with T cell polarization in vivo. *J. Clin.*
730 *Invest.* 108:1331–1339.

731 Klemann, C., L. Wagner, M. Stephan, and S. von Hörsten. 2016. Cut to the chase: a review of

CD26/dipeptidyl peptidase-4's (DPP4) entanglement in the immune system. *Clin. Exp. Immunol.* 185:1–21. doi:10.1111/cei.12781.

Kourelis, T. V, J.C. Villasboas, E. Jessen, S. Dasari, A. Dispenzieri, and D. Jevremovic. 2019. Mass cytometry dissects T cell heterogeneity in the immune tumor microenvironment of common dysproteinemias at diagnosis and after fi rst line therapies. *Blood Cancer J.* 9. doi:10.1038/s41408-019-0234-4.

Latorre, I., M.A. Fernández-Sanmartín, B. Muriel-Moreno, R. Villar-Hernández, S. Vila, M.L. De Souza-Galvão, Z. Stojanovic, M.A. Jiménez-Fuentes, C. Centeno, J. Ruiz-Manzano, J.-P. Millet, I. Molina-Pinargote, Y.D. González-Díaz, A. Lacoma, L. Luque-Chacón, J. Sabriá, C. Prat, and J. Domínguez. 2019. Study of CD27 and CCR4 Markers on Specific CD4+ T-Cells as Immune Tools for Active and Latent Tuberculosis Management. *Front. Immunol.* 9:1–11. doi:10.3389/fimmu.2018.03094.

Leipold, M.D., E.W. Newell, and H.T. Maecker. 2015. Multiparameter Phenotyping of Human PBMCs Using Mass Cytometry. *Methods Mol Biol.* 1343:1–14. doi:10.1007/978-1-4939-2963-4.

Lewinsohn, D.A., G.M. Swarbrick, B. Park, M.E. Cansler, M.D. Null, K.G. Toren, J. Baseke, S. Zalwango, H. Mayanja-Kizza, L.L. Malone, M. Nyendak, G. Wu, K. Guinn, S. McWeeney, T. Mori, K.A. Chervenak, D.R. Sherman, W.H. Boom, and D.M. Lewinsohn. 2017. Comprehensive definition of human immunodominant CD8 antigens in tuberculosis. *npj Vaccines*. 2:1–10. doi:10.1038/s41541-017-0008-6.

Lienhardt, C., K. Lönnroth, D. Menzies, M. Balasegaram, J. Chakaya, F. Cobelens, J. Cohn, C.M. Denkinger, T.G. Evans, G. Källenius, G. Kaplan, A.M.V. Kumar, L. Matthiessen, C.S. Mgone, V. Mizrahi, Y. diul Mukadi, V.N. Nguyen, A. Nordström, C.F. Sizemore, M. Spigelman, S.B. Squire, S. Swaminathan, P.D. Van Helden, A. Zumla, K. Weyer, D. Weil, and M. Raviglione. 2016. Translational Research for Tuberculosis Elimination:

Priorities, Challenges, and Actions. *PLoS Med.* 13:1–11. doi:10.1371/journal.pmed.1001965.

Lin, P.L., and J.L. Flynn. 2015. CD8 T cells and Mycobacterium tuberculosis infection. *Semin Immunopathol.* 37:239–249. doi:10.1007/s00281-015-0490-8.

Lindestam Arlehamn, C.S., A. Gerasimova, F. Mele, R. Henderson, J. Swann, J.A. Greenbaum, Y. Kim, J. Sidney, E.A. James, R. Taplitz, D.M. McKinney, W.W. Kwok, H. Grey, F. Sallusto, B. Peters, and A. Sette. 2013. Memory T Cells in Latent Mycobacterium tuberculosis Infection Are Directed against Three Antigenic Islands and Largely Contained in a CXCR3+CCR6+ Th1 Subset. *PLoS Pathog.* 9. doi:10.1371/journal.ppat.1003130.

De Maio, F., F. Squeglia, D. Goletti, and G. Delogu. 2018. The Mycobacterial HBHA Protein: A Promising Biomarker for Tuberculosis. *Curr. Med. Chem.* 26:2051–2060. doi:10.2174/0929867325666181029165805.

Marriott, I., R. Stephens, C.J. Serrano, M.L. Gennaro, R. Arrigucci, K. Lakehal, P. Vir, D. Handler, A.L. Davidow, R. Herrera, J. Dolores Estrada-Guzmán, Y. Bushkin, S. Tyagi, and A.A. Lardizabal. 2018. Active Tuberculosis Is Characterized by Highly Differentiated Effector Memory Th1 Cells. *Front. Immunol.* 9:2127. doi:10.3389/fimmu.2018.02127.

Masungi, C., S. Temmerman, J.P. Van Vooren, A. Drowart, K. Pethe, F.D. Menozzi, C. Locht, and F. Mascart. 2002. Differential T and B cell responses against Mycobacterium tuberculosis heparin-binding hemagglutinin adhesin in infected healthy individuals and patients with tuberculosis. *J. Infect. Dis.* 185:513–520. doi:10.1086/338833.

Mei, H.E., M.D. Leipold, A.R. Schulz, C. Chester, and H.T. Maecker. 2015. Barcoding of Live Human Peripheral Blood Mononuclear Cells for Multiplexed Mass Cytometry. *J. Immunol.* 194:2022–2031. doi:10.4049/jimmunol.1402661.

782 Moguche, A.O., M. Musvosvi, A. Penn-Nicholson, C.R. Plumlee, H. Mearns, H. Geldenhuys,
783 E. Smit, D. Abrahams, V. Rozot, O. Dintwe, S.T. Hoff, I. Kromann, M. Ruhwald, P.
784 Bang, R.P. Larson, S. Shafiani, S. Ma, D.R. Sherman, A. Sette, C.S. Lindestam
785 Arlehamn, D.M. McKinney, H. Maecker, W.A. Hanekom, M. Hatherill, P. Andersen,
786 T.J. Scriba, and K.B. Urdahl. 2017. Antigen Availability Shapes T Cell Differentiation
787 and Function during Tuberculosis. *Cell Host Microbe*. 21:695-706.e5.
788 doi:10.1016/j.chom.2017.05.012.
789 Musvosvi, M., D. Duffy, E. Filander, H. Africa, S. Mabwe, L. Jaxa, N. Bilek, A. Llibre, V.
790 Rouilly, M. Hatherill, M. Albert, T.J. Scriba, and E. Nemes. 2018. T-cell biomarkers for
791 diagnosis of tuberculosis: candidate evaluation by a simple whole blood assay for
792 clinical. *Eur Respir J*. 51. doi:10.1183/13993003.00153-2018.
793 Nyendak, M.R., B. Park, M.D. Null, J. Baseke, G. Swarbrick, H. Mayanja-Kizza, M. Nsereko,
794 D.F. Johnson, P. Gitta, A. Okwera, S. Goldberg, L. Bozeman, J.L. Johnson, W.H. Boom,
795 D.A. Lewinsohn, and D.M. Lewinsohn. 2013. Mycobacterium tuberculosis specific
796 CD8+ T cells rapidly decline with antituberculosis treatment. *PLoS One*. 8.
797 doi:10.1371/journal.pone.0081564.
798 Ohnuma, K., N.H. Dang, and C. Morimoto. 2008. Revisiting an old acquaintance: CD26 and
799 its molecular mechanisms in T cell function. *Trends Immunol.* 29:295–301.
800 doi:10.1016/j.it.2008.02.010.
801 Parrish, N.M., and K.C. Carroll. 2011. Role of the clinical mycobacteriology laboratory in
802 diagnosis and management of tuberculosis in low-prevalence settings. *J. Clin. Microbiol.*
803 49:772–776. doi:10.1128/JCM.02451-10.
804 Patankar, Y.R., R. Sutiwisesak, S. Boyce, R. Lai, C.S. Lindestam Arlehamn, A. Sette, and
805 S.M. Behar. 2020. Limited recognition of Mycobacterium tuberculosis-infected
806 macrophages by polyclonal CD4 and CD8 T cells from the lungs of infected mice.

807 *Mucosal Immunol.* 13:140–148. doi:10.1038/s41385-019-0217-6.

808 Pereira, D.G., A. Afonso, and F.M. Medeiros. 2015. Overview of Friedmans Test and Post-
809 hoc Analysis. *Commun. Stat. Simul. Comput.* 44:2636–2653.
810 doi:10.1080/03610918.2014.931971.

811 Petruccioli, E., T. Chiacchio, I. Pepponi, V. Vanini, R. Urso, G. Cuzzi, L. Barcellini, D.M.
812 Cirillo, F. Palmieri, G. Ippolito, and D. Goletti. 2016. First characterization of the CD4
813 and CD8 T-cell responses to QuantiFERON-TB Plus. *J. Infect.* 73:588–597.
814 doi:10.1016/j.jinf.2016.09.008.

815 Petruccioli, E., L. Petrone, V. Vanini, A. Sampaolesi, G. Gualano, E. Girardi, F. Palmieri, and
816 D. Goletti. 2013. IFNγ/TNFα specific-cells and effector memory phenotype associate
817 with active tuberculosis. *J. Infect.* 66:475–486. doi:10.1016/j.jinf.2013.02.004.

818 Qiagen. 2017. QuantiFERON®-TB Gold Plus (QFT®-Plus) Package Insert. 96:1101062.
819 doi:10.1016/j.athoracsur.2015.08.092.

820 Quintelier, K., A. Couckuyt, A. Emmaneel, J. Aerts, Y. Saeys, and S. Van Gassen. 2021.
821 Analyzing high-dimensional cytometry data using FlowSOM. *Nat. Protoc.*
822 doi:10.1038/s41596-021-00550-0.

823 Rahman, A.H., L. Tordesillas, and M.C. Berin. 2016. Heparin Reduces Nonspecific
824 Eosinophil Staining Artifacts in Mass Cytometry Experiments. *Cytometry*. 89A:601–
825 607. doi:10.1002/cyto.a.22826.

826 Riou, C., N. Berkowitz, R. Goliath, W.A. Burgers, and R.J. Wilkinson. 2017. Analysis of the
827 phenotype of Mycobacterium tuberculosis-specific CD4+ T cells to discriminate latent
828 from active tuberculosis in HIV-Uninfected and HIV-Infected individuals. *Front.*
829 *Immunol.* 8. doi:10.3389/fimmu.2017.00968.

830 Riou, C., E. Du Bruyn, S. Ruzive, R.T. Goliath, C.S. Lindestam Arlehamn, A. Sette, A. Sher,
831 D.L. Barber, and R.J. Wilkinson. 2020. Disease extent and anti-tubercular treatment

response correlates with *Mycobacterium tuberculosis*-specific CD4 T-cell phenotype regardless of HIV-1 status. *Clin. Transl. Immunol.* 9:e1176. doi:10.1002/cti2.1176.

Riou, C., C.M. Gray, M. Lugongolo, T. Gwala, A. Kiravu, P. Deniso, L. Stewart-Isherwood, S.V. Omar, M.P. Grobusch, G. Coetzee, F. Conradie, N. Ismail, G. Kaplan, and D. Fallows. 2014. A subset of circulating blood mycobacteria-specific CD4 T cells can predict the time to Mycobacterium tuberculosis sputum culture conversion. *PLoS One*. 9. doi:10.1371/journal.pone.0102178.

Roy Chowdhury, R., F. Vallania, Q. Yang, C.J. Lopez Angel, F. Darboe, A. Penn-Nicholson, V. Rozot, E. Nemes, S.T. Malherbe, K. Ronacher, G. Walzl, W. Hanekom, M.M. Davis, J. Winter, X. Chen, T.J. Scriba, P. Khatri, and Y. Chien. 2018. A multi-cohort study of the immune factors associated with M. tuberculosis infection outcomes. *Nature*. doi:10.1038/s41586-018-0439-x.

Rozot, V., S. Vigano, J. Mazza-stalder, E. Idrizi, C.L. Day, M. Perreau, C. Lazor-blanchet, E. Petruccioli, W. Hanekom, P. Bart, L. Nicod, G. Pantaleo, and A. Harari. 2013. Mycobacterium tuberculosis-specific CD8+ T cells are functionally and phenotypically different between latent infection and active disease. *Eur. J. Immunol.* 43:1568–1577. doi:10.1002/eji.201243262.Mycobacterium.

Rubin, S.J.S., L. Bai, Y. Haileselassie, G. Garay, C. Yun, L. Becker, S.E. Streett, S.R. Sinha, and A. Habtezion. 2019. Mass cytometry reveals systemic and local immune signatures that distinguish inflammatory bowel diseases. *Nat. Commun.* 10. doi:10.1038/s41467-019-10387-7.

Sali, M., D. Buonsenso, P. D'Alfonso, F. De Maio, M. Ceccarelli, B. Battah, I. Palucci, T. Chiacchio, D. Goletti, M. Sanguinetti, P. Valentini, and G. Delogu. 2018. Combined use of Quantiferon and HBHA-based IGRA supports tuberculosis diagnosis and therapy management in children. *J. Infect.* doi:10.1016/j.jinf.2018.09.011.

857 Serbina, N. V., C.-C. Liu, C.A. Scanga, and J.L. Flynn. 2000. CD8+ CTL from Lungs of
858 Mycobacterium tuberculosis -Infected Mice Express Perforin In Vivo and Lyse Infected
859 Macrophages. *J. Immunol.* 165:353–363. doi:10.4049/jimmunol.165.1.353.
860 Singhania, A., R. Verma, C.M. Graham, J. Lee, T. Tran, M. Richardson, P. Lecine, P.
861 Leissner, M.P.R. Berry, R.J. Wilkinson, K. Kaiser, M. Rodrigue, G. Woltmann, P.
862 Haldar, and A. O'Garra. 2018. A modular transcriptional signature identifies phenotypic
863 heterogeneity of human tuberculosis infection. *Nat. Commun.* 9. doi:10.1038/s41467-
864 018-04579-w.
865 Vickers, M.A., F. Darboe, C.N. Muefong, G. Mbayo, A. Barry, A. Gindeh, S. Njie, A.J.
866 Riley, B. Sarr, B. Sambou, H.M. Dockrell, S. Charalambous, A. Rachow, O. Owolabi, S.
867 Jayasooriya, and J.S. Sutherland. 2020. Monitoring Anti-tuberculosis Treatment
868 Response Using Analysis of Whole Blood Mycobacterium tuberculosis Specific T Cell
869 Activation and Functional Markers. *Front. Immunol.* 11:1–13.
870 doi:10.3389/fimmu.2020.572620.
871 Wang, X., Z. Cao, J. Jiang, H. Niu, M. Dong, A. Tong, and X. Cheng. 2010. Association of
872 mycobacterial antigen-specific CD4+ memory T cell subsets with outcome of pulmonary
873 tuberculosis. *J. Infect.* 60:133–139. doi:10.1016/j.jinf.2009.10.048.
874 World Health Organization Geneva. 2018. Global Tuberculosis Report 2018.
875 World Health Organization Geneva. 2019. WHO consolidated guidelines on drug-resistant
876 tuberculosis treatment.
877 World Health Organization Geneva. 2020. Global Tuberculosis Report 2020. 1. 1–8 pp.
878 Yoav Benjamini, and Yosef Hochberg. 1995. Controlling the False Discovery Rate: A
879 Practical and Powerful Approach to Multiple Testing. *J. R. Stat. Soc. Ser. B.* 57:289–300.
880

881

Figures

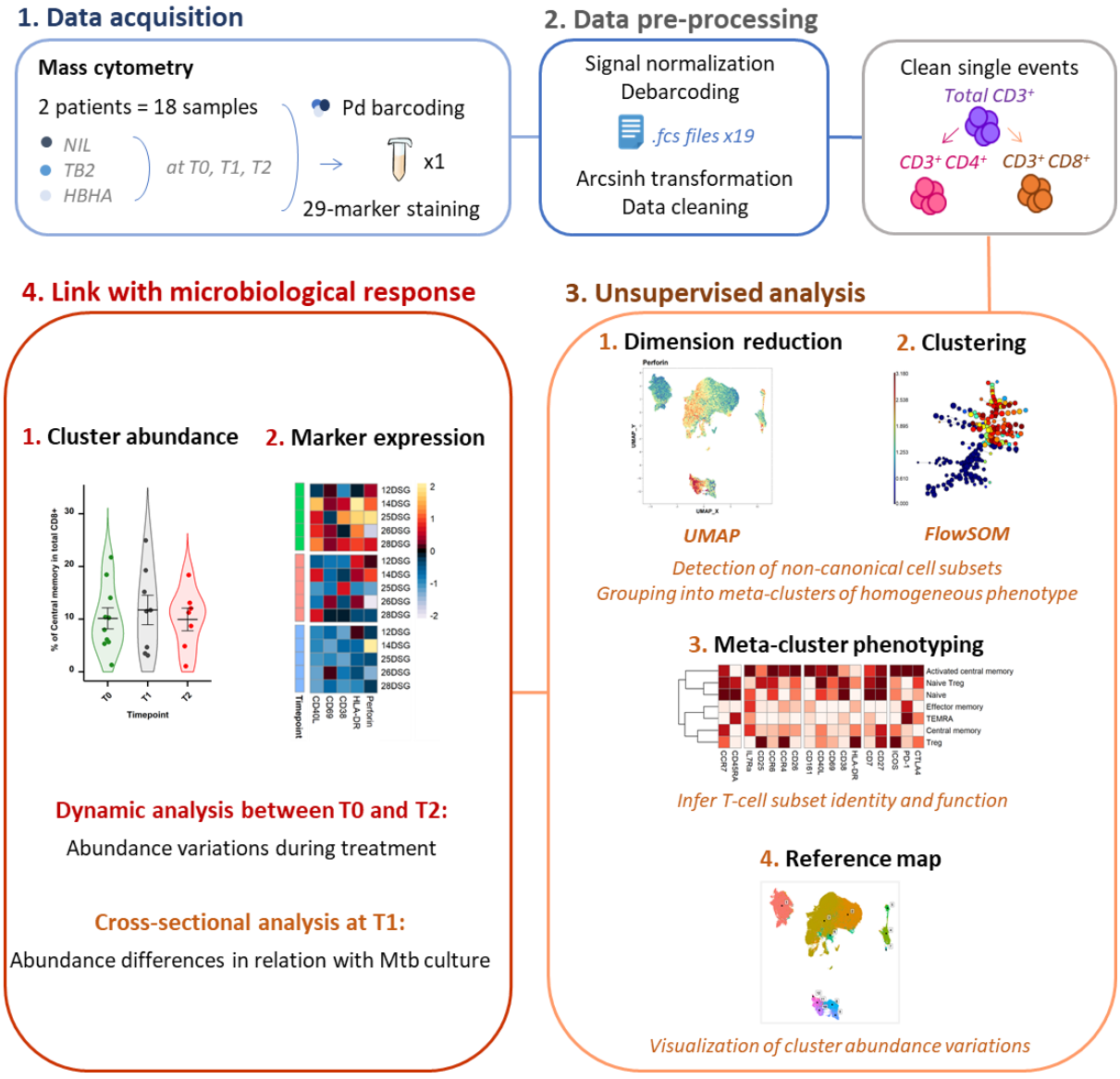

Figure 1. Experimental and analytical workflow.

Peripheral whole blood samples were collected from active TB patients (n = 22) throughout treatment (T0: baseline. T1: T0 + 2 months. T2: end of treatment). After whole blood stimulation with *Mtb* antigens (TB2 and rmsHBHA) or with a negative control (NIL), total white blood cells were extracted. After palladium (Pd) barcoding for unique sample identification before multiplexing, T-cells were analyzed with a 29-marker mass cytometry panel. Abbreviations: TB2: Qiagen QuantiFERON TB2 tube (ESAT-6 + CFP-10 + undisclosed

891 $CD8^+$ T-cell stimulating peptide pool). rmsHBHA: recombinant heparin-binding hemagglutinin
892 obtained in *Mycobacterium smegmatis*. UMAP: Uniform Manifold Approximation and
893 Projection. FlowSOM: self-organizing map.

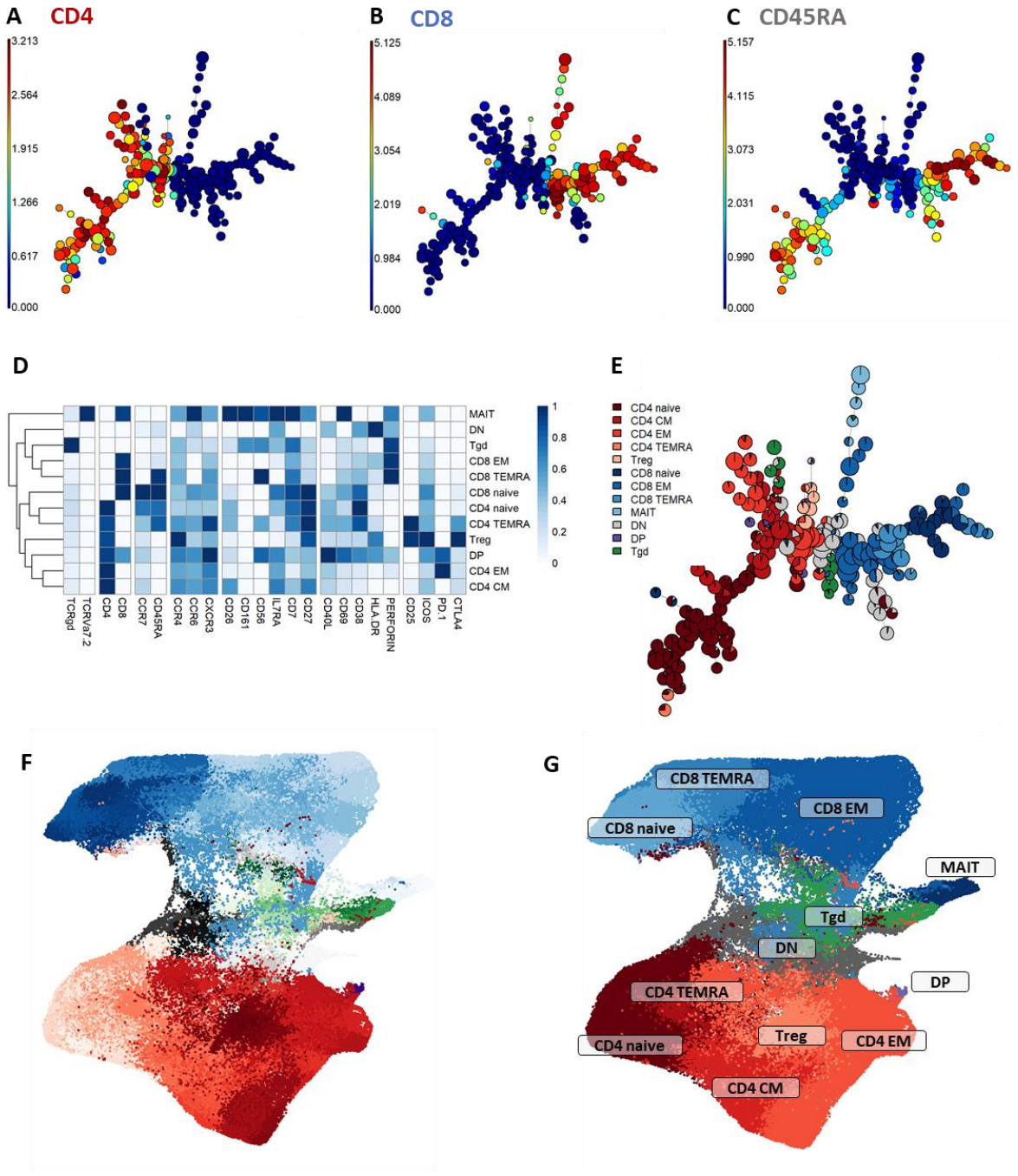

Figure 2. Peripheral CD3$^+$ T-cell unsupervised clustering and phenotyping.

A to E. FlowSOM automated clustering. The surface expression of lineage markers used for FlowSOM calculations was visualized in all CD3$^+$ events (201,000 events from equally down-sampled files) regardless of timepoint or stimulation. FlowSOM enabled automated repartition of CD3$^+$ events into 196 clusters according to the surface expression of selected lineage markers such as CD4 (**A**), CD8 (**B**), and CD45RA (**C**). Scales indicate arcsinh-transformed mass signal

values. Clusters were automatically grouped into 18 meta-clusters of homogeneous phenotype, which were assembled into 12 canonical T-cell subpopulations in a supervised manner after meta-cluster phenotyping. This was performed with heatmap visualization of normalized, arcsinh-transformed median mass signal values for each surface marker (**D**). The proportions of the resulting T-cell subpopulations were visualized on the initial FlowSOM minimum spanning tree to control phenotyping consistency (**E**).

F and G. Reference mapping. Dimension reduction was performed with UMAP and overlayed with automatically determined FlowSOM clusters (**F**) and meta-clusters (**G**) to generate a phenotype reference map. Cluster labels were not displayed for legibility. Abbreviations: CM: central memory. DN: double-negative $CD4^{-}CD8^{-}$. DN: double-positive $CD4^{+}$ $CD8^{+}$. EM: effector memory. MAIT: mucosal associated invariant T-cells. Tgd: gamma delta T-cells. Treg: T-regulators. TEMRA: terminally differentiated effectors re-expressing CD45RA.

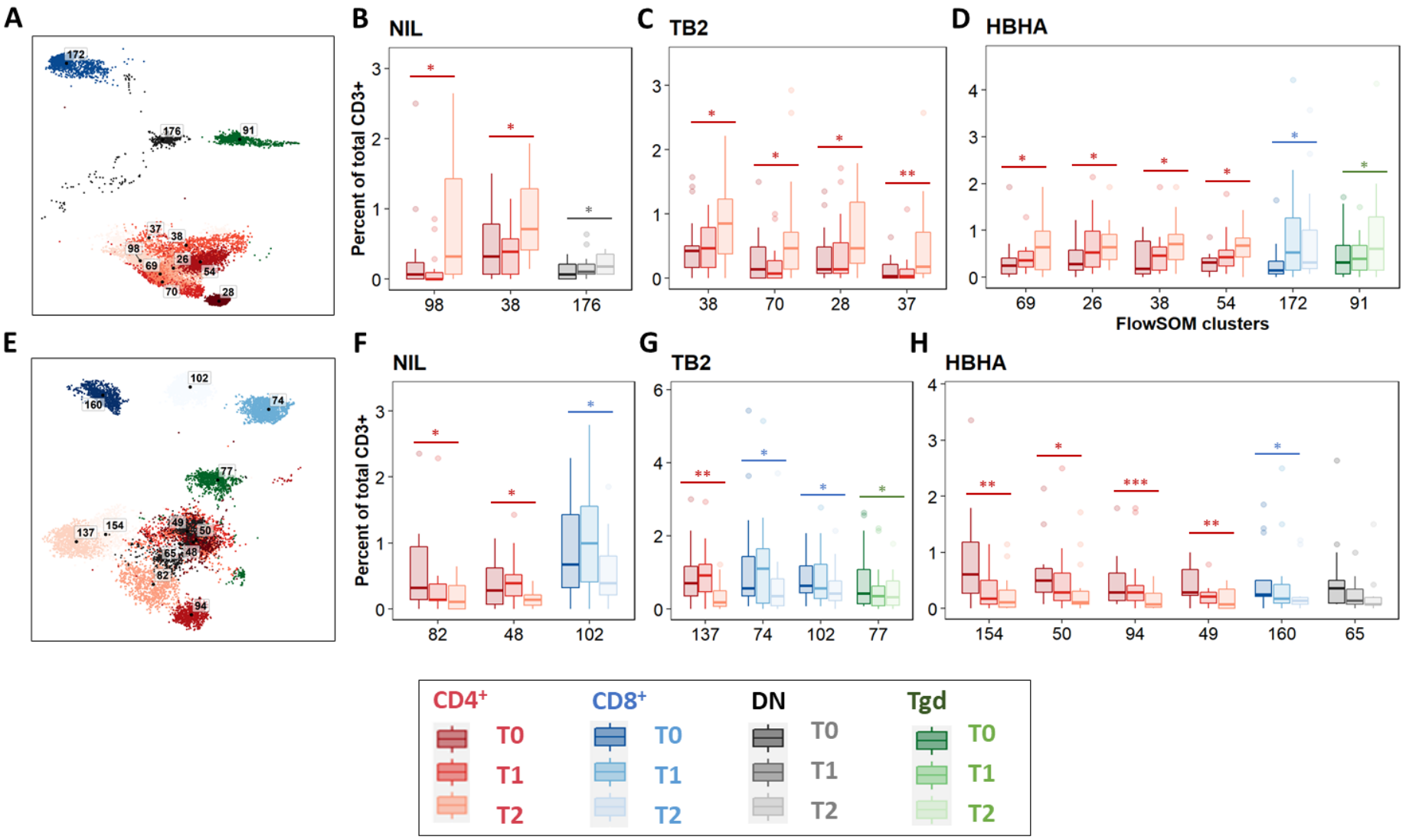

913

914 **Figure 3. Significant abundance changes in non-canonical T-cell subsets throughout TB treatment.**

FlowSOM cluster abundance was analyzed over time in unstimulated or *Mtb*-stimulated samples (TB2 or rmsHBHA). Only clusters within which significant abundance changes were detected were displayed. Number of matched data points per timepoint for all panels: NIL: n = 16. TB2: n = 18. rmsHBHA: n = 14. Data are represented as medians + interquartile range.

A to D. Significantly increased clusters at treatment completion (T2) compared to treatment initiation (T0). Clusters within which a significant increase was detected between T0 and T2 were visualized on the reference UMAP shown in Figure 3 (**A**). Cluster abundance quantification was was performed in unstimulated (**B**), TB2-stimulated (C) or rmsHBHA-stimulated samples (**D**).

E to H. Significantly decreased clusters at treatment completion (T2) compared to treatment initiation (T0). Mapping (**E**) and abundance quantification of clusters which increased between T0 and T2 in unstimulated (**F**), TB2-stimulated (**G**) or rmsHBHA-stimulated samples (**H**).

Abbreviations: DN: double negative $CD4^-$ $CD8^-$. Tgd: gamma delta T-cells. Statistical analysis: Friedman rank sum test and Wilcoxon-Nemenyi-Thompson post-hoc for pairwise comparisons between non-independent observations at T0, T1, and T2. *: $p<0.05$. **: $p<0.01$. ***: $p<0.001$. Exact p-values and test statistics are available in Supp. Table 3.

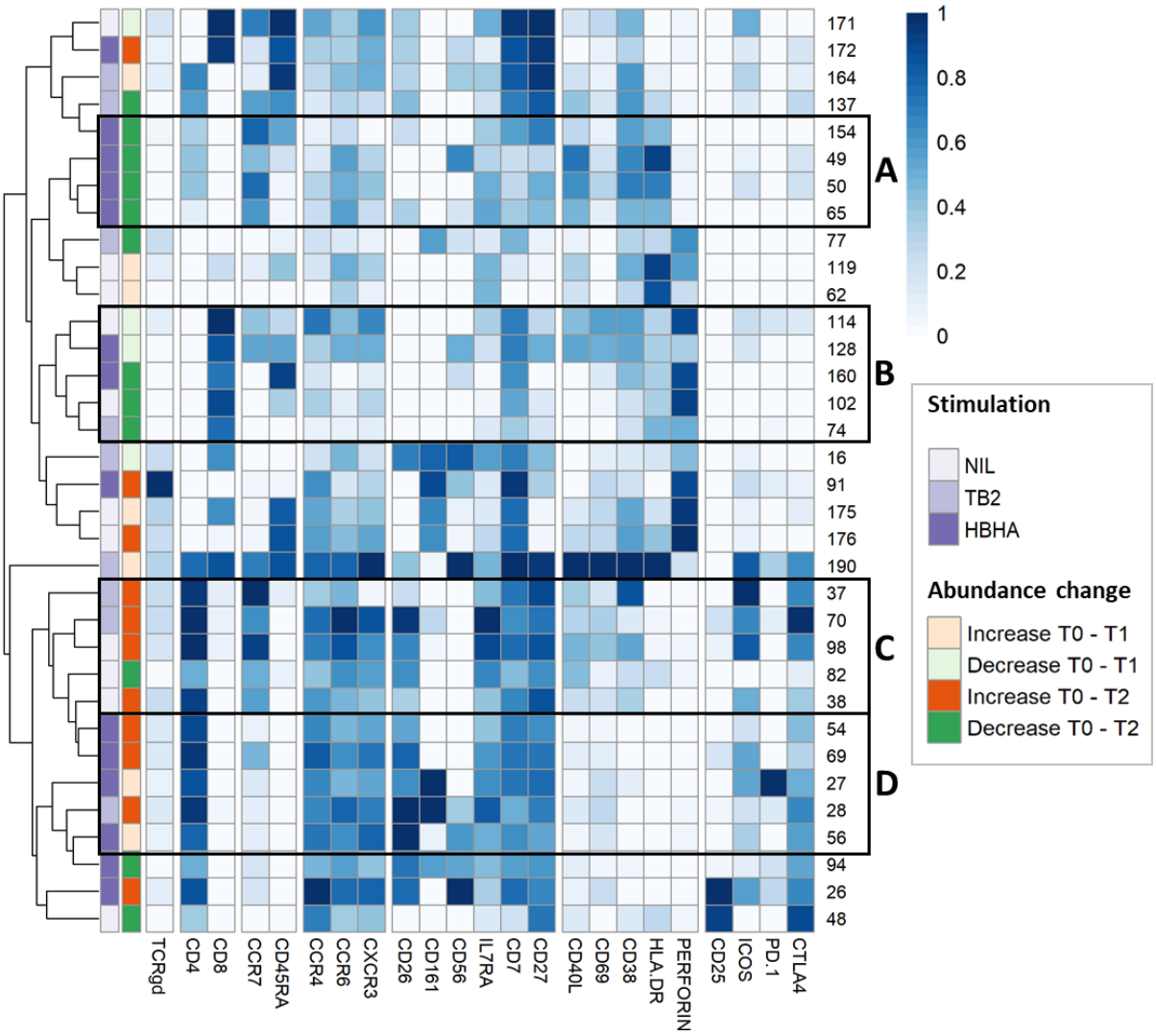

Figure 4. In-depth phenotyping shows differential involvement of effector and memory T-cells in antigen-driven cluster abundance changes during TB treatment.

Mean marker expression levels were visualized using heatmapping for cell cluster which increased (orange color code) or decreased (green color code) throughout treatment. Each line represents one cell cluster. Scales indicate normalized mass signal intensity. Hierarchical clustering was performed based on marker expression levels, regrouping cell clusters of similar immunophenotypes. Black rectangles annotated from A to D indicate cell cluster subgroups with both similar immunophenotypes and abundance changes.

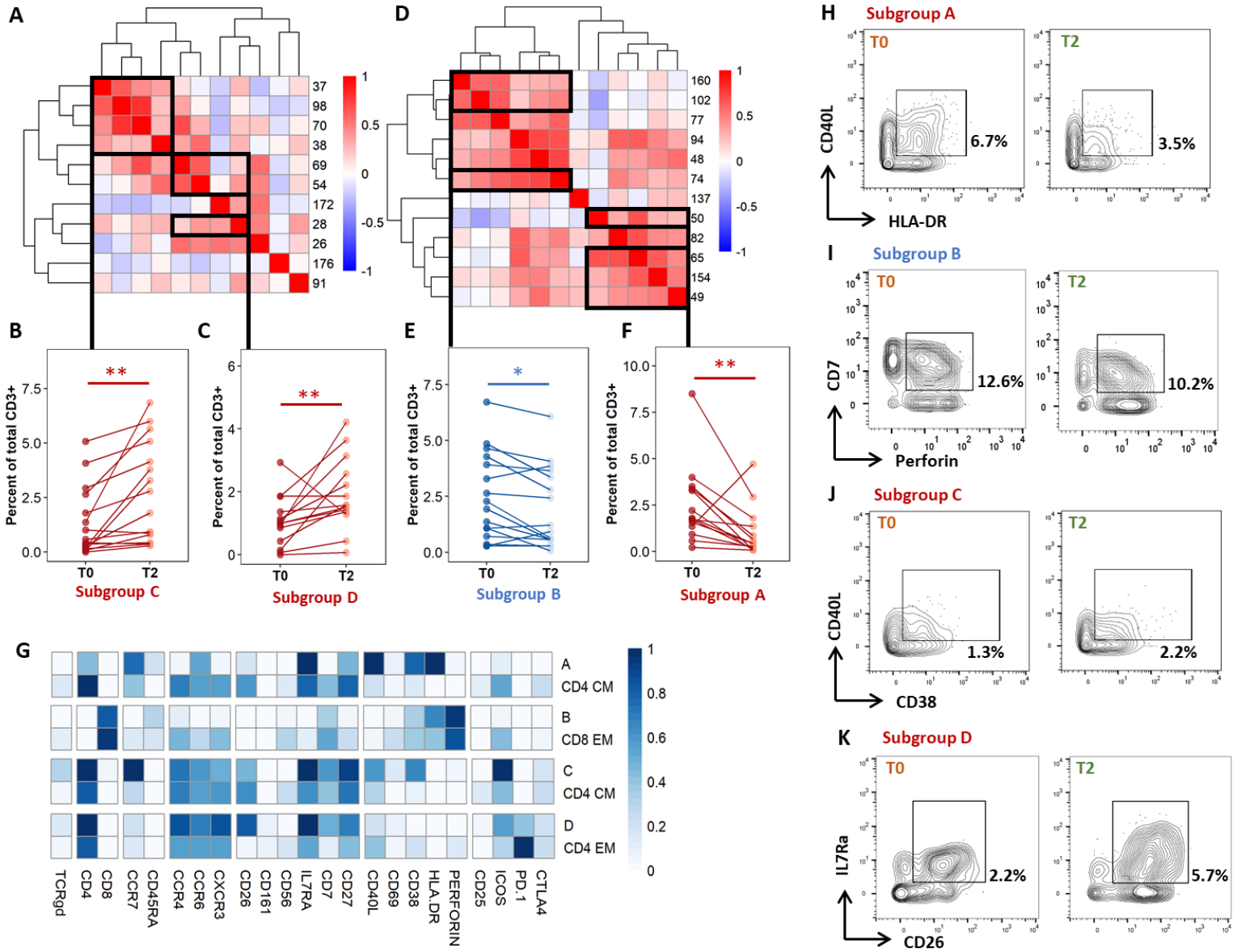
A
37
98
70
38
69
54
172
28
26
176
91
1
0.5
0
-0.5
-1
D
160
102
77
94
48
74
137
50
82
65
154
49
B
C
E
F
Percent of total CD3+
**
**
*
**
T0
T2
Subgroup C
Subgroup D
Subgroup B
Subgroup A
G
A
CD4 CM
B
CD8 EM
C
CD4 CM
D
CD4 EM
TCRgd
CD4
CD8
CCR7
CD45RA
CCR4
CCR6
CXCR3
CD26
CD161
CD56
IL7RA
CD7
CD27
CD40L
CD69
CD38
HLA.DR
PERFORIN
CD25
ICOS
PD.1
CTLA4
H
Subgroup A
T0
T2
CD40L
6.7%
3.5%
HLA-DR
I
Subgroup B
CD7
12.6%
10.2%
Perforin
J
Subgroup C
CD40L
1.3%
2.2%
CD38
K
Subgroup D
IL7Ra
2.2%
5.7%
CD26

936

Figure 5. Individual immunoprofiling confirms differential abundance of correlated subsets in cured patients after treatment.

Cluster were stratified by type of significant abundance change: enrichment (**A to C**) or depletion (**D to F**) after treatment completion.

A and D. Pearson's correlations were calculated on cluster abundance at T0 and displayed on a heatmap with hierarchical clustering. Clusters with similar immunophenotypes (Figures 3 and 4) and positive correlation coefficients were grouped. Estimates of effect sizes are in Supp. Tables 4 and 5.

B, C, E, F. The abundance of each subgroup was visualized. Each dot represents data for one patient. Statistical analysis: Friedman rank sum test. *: $p<0.05$. **: $p<0.01$. Subgroup A: data from rmsHBHA samples (n =14), clusters 49, 50, 65, 154; p = 0.0013, Friedman's Chi-Square (Fchisq) = 10.3. Subgroup B: data from unstimulated samples (n =16), clusters 74, 102, 160; p = 0.020, Fchisq = 5.4. Subgroup C: data from unstimulated samples, clusters 37, 38, 70, 98; p = 0.0027, Fchisq = 9. Subgroup D: data from rmsHBHA samples, clusters 28, 54, 69; p = 0.0023, Fchisq = 9.3.

F. For each subgroup, normalized mean marker expression levels were compared with similar T-cell subsets.

G to K. Manual gating analysis was performed to verify unsupervised results (representative plots, 500 to 1,000 events). Numbers indicate the percentage of gated cells among total $CD3^+$ cells. Subgroup A: $CD4^+CCR7^+CD45RA^-CCR6^+IL7Ra^+CD27^+CD40L^+CD38^+HLA\text{-}DR^+$. Subgroup B: $CD8^+CCR7^-CD45RA^-CD7^+$ $Perforin^+$. Subgroup C: $CD4^+CCR7$ $CD45RA^-CCR4^+CCR6^+CXCR3^+CD26^+IL7Ra^+CD7^+CD27^+$ $CD40L^+CD38^+$. Subgroup D: $CD4^+CCR7^-CD45RA^-CCR4^+CCR6^+$ $CXCR3^+CD26^+IL7Ra^+CD7$ $CD27^+CD40L^+CD38^+$ $HLA\text{-}DR^-$.

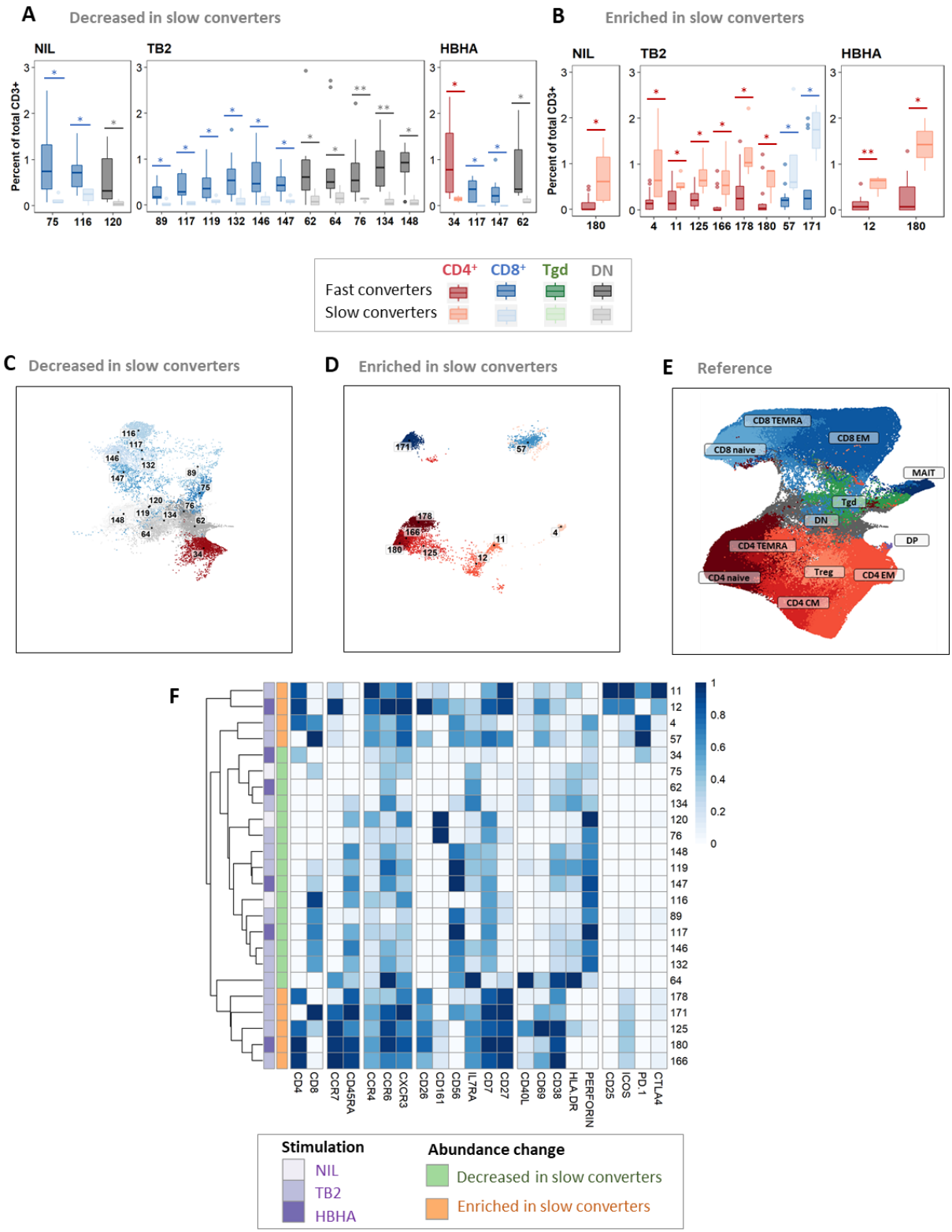

Figure 6. Patients with slow microbiological culture conversion show decreased cytotoxic CD8$^+$ and γδ enriched CD4$^+$ naïve T-cell subsets before treatment initiation and after two months of treatment compared to fast converters.

Fast converters (n = 18) were defined as patients with permanently negative *M. tuberculosis* culture after two months of treatment (T1), whereas slow converters (n = 4) were defined as patients with persistently positive cultures at T1. The abundance of all FlowSOM clusters at baseline was compared between fast and slow converters. $CD4^+$ clusters were represented in red, $CD8^+$ clusters in blue, and γδ T-cell clusters in green. Clusters which were significantly decreased (**A** and **C**) or enriched (**B** and **D**) at T1 in slow converters compared to fast converters were compared to the reference UMAP (**E**). Normalized, arcsinh-transformed mean marker expression levels were visualized (**F**). Each row represents one cluster. Scales indicate normalized mass signal intensity. Boxplot data represent medians + interquartile range.

Statistical analysis: Only clusters within which significant differences were detected were represented. Significance threshold: $p<0.035$ (Mann-Whitney U test). *: $p<0.031$. **: $p<0.001$. Exact p-values and test statistics are available in Supp. Table 6.

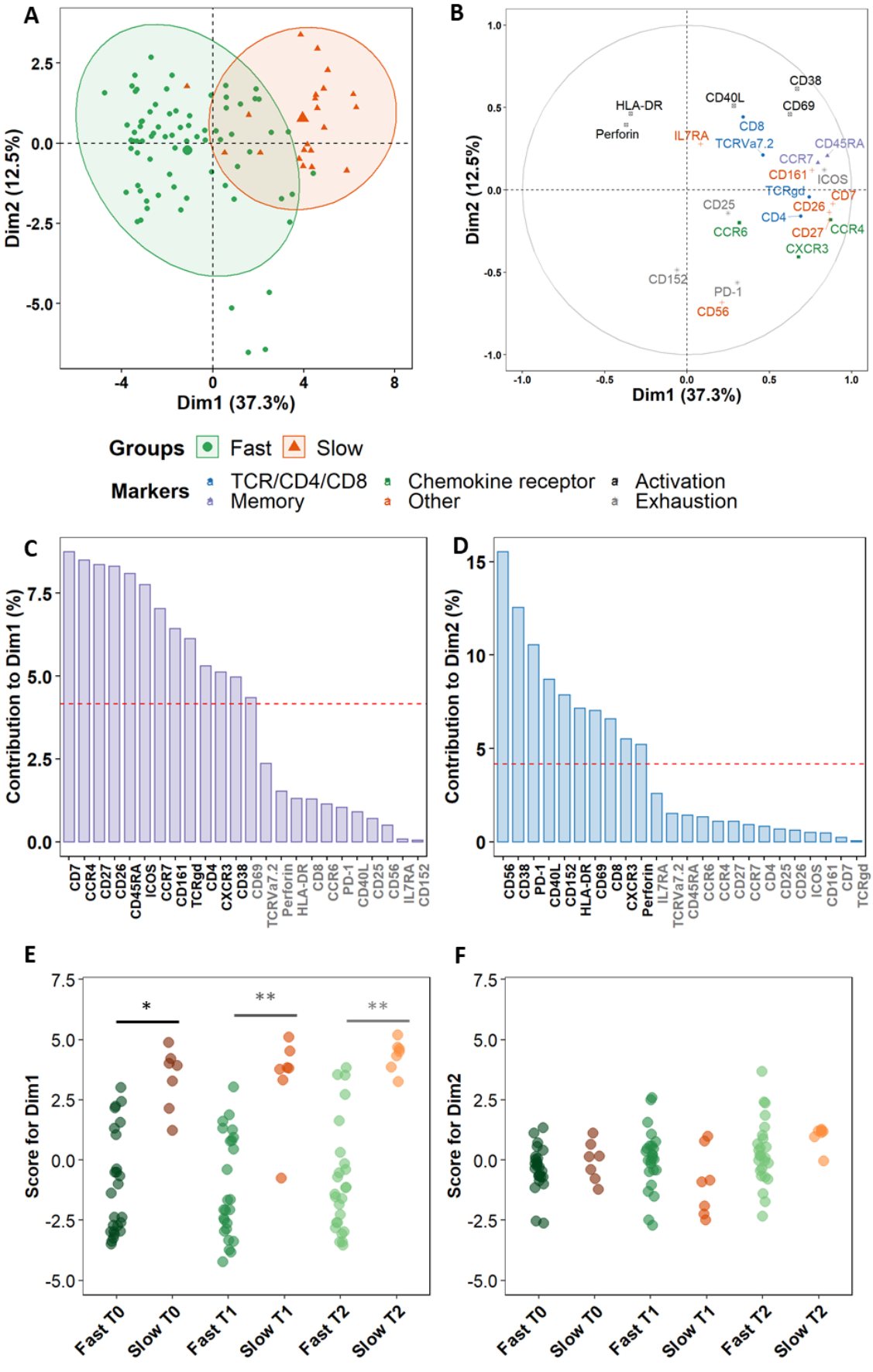

969

970 **Figure 7. Non-lineage markers discriminate slow and fast responders within differentially**
971 **abundant subsets.**

972 Principal Component Analysis (PCA) was performed on marker expression data from the
973 clusters identified in Figure 6, within 96 *Mtb*-stimulated samples matched at T0, T1, and T2
974 (TB2: 54 samples; rmsHBHA: 42 samples; see Supp. Table 1 for sample number details).

975 **A.** Explanation of the variance between fast converters (25 samples at each timepoint) and slow
976 converters (7 samples at each timepoint). Axes represent the principal components 1
977 (Dimension 1, Dim1) and 2 (Dim2). Percentages indicate their contribution to the total observed
978 variance. Axis values represent individual PCA scores. Concentration ellipses correspond to
979 90% data coverage.

980 **B.** Contribution of cellular markers to the variance described by Dim1 and Dim2. Axis values
981 represent marker PCA scores. Color codes represent broad marker functions.

982 **C and D.** Quantification of panel B for Dim1 (**C**) and Dim2 (**D**). Contributions of each marker
983 are expressed as a percentage of the dimensions. The dashed line corresponds to the expected
984 reference value if each marker contributed uniformly to the variance. Markers indicated in gray
985 are below this reference value.

986 **E and F.** Distribution of individual PCA score values according to the culture conversion group
987 at each timepoint, for Dim1 (**E**) and Dim2 (**F**). Wilcoxon Rank Sum Test. ***: $p<0.001$. **:
988 $p<0.001$. Exact p-values and test statistics are in Supp. Table 7.

989

Tables

Table 1. Selected subset abundance changes before and after treatment completion.

Sample	Abundance between T0 and T2 (%, N)
Subset A decreased	
NIL (n=16)	62% (10)
TB2 (n=18)	67% (12)
rmsHBHA (n=14)	**93% (13)**
Subset B decreased	
NIL	**81% (13)**
TB2	72% (13)
rmsHBHA	71% (10)
Subset C increased	
NIL	**88% (14)**
TB2	72% (13)
rmsHBHA	57% (8)
Subset D increased	
NIL	69% (11)
TB2	78% (14)
rmsHBHA	**93% (13)**

Footnotes: these data were obtained from Figure 5.

Table 2. Proportions of the main T-cell subpopulations within enriched or decreased subsets in slow converters compared to fast converters.

	T0 (21 clusters)		T1 (24 clusters)		T2 (21 clusters)	
Abundance in slow vs. fast converters	**Decreased**	**Enriched**	**Decreased**	**Enriched**	**Decreased**	**Enriched**
	86% (18)	**14% (3)**	**62% (15)**	**38% (9)**	**52% (11)**	**48% (10)**
Total $CD8^+$ and γδ	**72% (13)**	**67% (2)**	**53% (8)**	**22% (2)**	**36% (4)**	**20% (2)**
γδ T-cells	38 (5)	-	-	-	-	-
$CD8^+$ TEMRA	24 (3)	50 (1)	75 (6)	-	-	-
$CD8^+$ EM	38 (5)	-	25 (2)	50 (1)	100 (4)	-
$CD8^+$ naïve	-	50 (1)	-	50 (1)	-	100 (2)
Total $CD4^+$	**11% (2)**	**33% (1)**	**7% (1)**	**78% (7)**	**36% (4)**	**80% (8)**
$CD4^+$ TEMRA	-	-	-	14 (1)	-	-
$CD4^+$ EM	50 (1)	-	100 (1)	29 (2)	100 (4)	-
$CD4^+$ CM	50 (1)	-	-	14 (1)	-	38 (3)
$CD4^+$ naïve	-	100 (1)	-	43 (3)	-	62 (5)
Total DN	**17% (3)**	**0**	**40% (6)**	**0**	**27% (3)**	**0**

Footnotes: these data were obtained from Figure 6 and Supp. Figure 6. Data are given as percentage of clusters in each category (number of clusters in each category/total number of decreased or enriched clusters).